

Master Thesis

**Exploring the existence of prebiotic species:
ALMA observations of amine-containing
organic molecule in star-forming regions.**

Harumi Minamoto

17M01629

Nomura Laboratory

Department of Earth and Planetary Sciences, Tokyo Institute of Technology

January 28, 2019

Abstract

A variety of complex organic molecules have been observed for decades in the interstellar medium. Some of them are considered to be delivered to the primordial Earth by comets, and contributed to the chemical evolution leading to terrestrial life. One example of such prebiotic species is amino acid. Glycine, the simplest amino acid, has been detected in comet 67P/C-G but its presence in molecular clouds is still uncertain.

In this work we analyze the ALMA archival data toward 3 star-forming regions, Orion Kleinmann-Low nebula (hereafter Orion-KL), IRAS 16293-2422 (IRAS 16293), and L483, to search methylamine (CH_3NH_2), which is suggested as precursors to glycine.

As a result of analysis, we found 6 candidate emission at the hot core region in Orion-KL. By using the rotation diagram method, we evaluated its tentative column density and rotational temperature to be $(5.5^{+1.6}_{-1.1}) \times 10^{14} \text{ cm}^{-2}$ and $95.4^{+15.5}_{-11.7} \text{ K}$, respectively.

On the other hand, CH_3NH_2 is not detected and stringent upper limit column densities are determined in IRAS 16293 and L483.

Contents

Abstract	i
1 Introduction	1
1.1 Glycine and methylamine	1
1.2 Star forming region	2
1.2.1 Orion Kleinmann-Low nebula	2
1.2.2 Low mass star-forming regions	2
1.3 Radio observation	3
1.3.1 Atacama Large Millimeter Array	4
1.4 Purpose of this work	4
2 Observation data & Analysis	5
2.1 Observation data	5
2.2 Analysis	6
2.2.1 Reduction of SV data	6
2.2.2 Line identification	10
3 Results	11
3.1 Overall CH ₃ NH ₂ distribution	11
3.2 Spectrum	20
4 Discussion	22
4.1 Column density and Rotation temperature	22

4.2 Suspicious lines	23
5 Conclusions	29
A Methylamine survey in low mass star-forming regions	30
A.1 IRAS 16293	31
A.1.1 Observation data	31
A.1.2 Results	31
A.2 L483	33
A.2.1 Observation data	33
A.2.2 Results	33
B Distribution of methylamine lines contaminated by other molecular line emission in Orion-KL	35
B.1 Integrated intensity maps	35
B.2 Channel maps	39
Acknowledgments	55
References	56

Chapter 1

Introduction

1.1 Glycine and methylamine

Methylamine (CH_3NH_2) is considered as a precursor of the simplest amino acid glycine. Recent experimental studies have shown several reaction pathways to forming glycine in water containing ices starting from CH_3NH_2 and CO_2 subjected to high energy electrons (Holtom et al., 2005) or UV radiation (Bossa et al., 2009; Lee et al., 2009). Under similar conditions glycine can decompose to yield methylamine and CO_2 (Ehrenfreund et al., 2001). Interstellar CH_3NH_2 was first detected toward Sgr B2 at 3.5 cm (Fourikis et al., 1974) and at 3mm (Kaifu et al., 1974). Recently, CH_3NH_2 has been detected in cometary samples of the Stardust mission (Glavin et al., 2008) and comet 67P/C-G (Altwegg et al., 2016, 2017).

1.2 Star forming region

1.2.1 Orion Kleinmann-Low nebula

This Orion Kleinmann-Low nebula (hereafter Orion-KL) to be studied is an infrared nebula in the Orion nebula, which is located approximately 388 ± 5 pc away from the sun (Kounkel et al., 2017). In this region, it is a very active area where a huge star with 30 times the mass of the sun is born, and a lot of molecules are observed also in line survey observing a wide range of frequencies. This Orion-KL is a large mass star formation region closest to the sun and has strong radiant intensity and still many molecules exist. Since this region was discovered in 1967, many studies including line survey have been done so far. In Orion-KL, a place called Hot core and Compact ridge is known as a region where many organic molecules exist. Hot core is known as a high-density (10^6 cm^{-3}) area with a warm ($\sim 150 \text{ K}$), compact ($< 0.05 \text{ pc}$), and Compact ridge is also known to be a warm and dense region. However, the chemical properties are different, while many molecules containing nitrogen (for example, NH_3 , CH_3CN , etc.) are observed in Hot core, while molecules containing oxygen (eg, CH_3OH , CH_3OCH_3 , etc.) are observed in Compact ridge.

1.2.2 Low mass star-forming regions

1.3 Radio observation

The observation of outer space by radio waves has been established as one of observation methods of outer space since the discovery of the first cosmic radio wave in the 1930s by Karl G. Jansky and the creation of the world's first radio telescope by Grote Reber. It has made great progress with the progress of radar technology during World War II. Since then, observations have been carried out even at wavelengths such as X-rays and infrared, unraveling the wonders of the universe that can not be known with only visible light. However, due to the influence of atmospheric absorption, visible light, radio waves and part of infrared rays are observable from the ground of all wavelengths. In the area of radio waves, frequencies below 20 MHz do not pass through the ionosphere, and at high frequencies they are easily absorbed by atmospheric oxygen and water vapor. For this reason, it is appropriate to install the radio telescope in places with high altitude and low water vapor. Different phenomena can be captured in outer space by the wavelengths observed, such as visible light and infrared light, but in observation of outer space by radio waves there is a feature not found in other wavelengths.

- We can observe low temperature objects that can not be seen with visible light.

After being born, the star radiates visible light, but low temperature objects before the star is born release not visible light but radio waves. Therefore, observations by radio waves is necessary.

- Long wavelength

Because of this feature, it is hard to be absorbed by interstellar microparticles, and it is possible to observe up to the far side.

- Easy electrical interference technology In a telescope called an interferometer, it is possible to obtain a high resolution by observing by placing a plurality of antennas apart and interfering radio waves. With this method in the radio wave range, higher resolution than observation with other wavelengths is obtained.

With the above characteristics, radio observation occupies an important position in astronomy.

1.3.1 Atacama Large Millimeter Array

1.4 Purpose of this work

This paper is organized as follows. In Section 2, we report the results of survey observations of CH₃NH₂ in Orion-KL.

地球で有機物が蓄積したもう一つの機構として、宇宙空間で合成された有機物が地球に持ち込まれた可能性がある。宇宙空間では様々な

Chapter 2

Observation data & Analysis

In this chapter, we report the tentatively detection CH₃NH₂ in Orion-KL.

2.1 Observation data

We analyzed 2 ALMA archival data. First we used Cycle 2 data (ADS/JAO.ALMA#2013.1.00553.S, Pagani et al. (2017)) We also employed the ALMA Science Verification (SV) data (ADS/JAO.ALMA#2011.0.00009.SV) at band 6 to fill up the missing frequency coverage of Cycle 2 data. Details of each data are summarized in Table 2.1.

Cycle 2 data cube was already calibrated by Pagani et al., and the reduced data are available on the web site of CDS (Centre de Donnees astronomiques de Strasbourg)¹. Since the SV data contained not only line emission but continuum emission, we subtracted continuum emission statistically by the method described in Section 2.2.1.

In addition, we used Common Astronomy Software Applications (CASA) software (McMullin et al., 2007) during the procedure to analyze observational data.

¹<http://cdsarc.u-strasbg.fr/viz-bin/qcat?J/A+A/604/A32>

Table 2.1: Summary of Observations

Date	Window (spw)	Frequency range (GHz)	FWHM (arcsec)	PA (degree)
29–30 December 2014	1	215.145–216.087	1.8×1.1	86
	2	216.342–217.279	1.8×1.1	84
	3	217.273–218.211	2.2×1.0	102
	4	218.204–219.141	2.2×1.0	102
	5	219.127–220.064	1.9×1.0	95
	6	219.784–220.721	1.8×1.0	95
	7	229.757–230.694	1.4×0.8	80
	8	230.699–231.636	2.1×0.9	102
	9	232.238–233.175	1.6×1.0	80
	10	233.470–234.422	1.6×0.8	90
	11	235.084–236.021	1.7×0.9	95
	12	236.267–237.206	1.6×0.9	87
	13	244.834–245.771	1.6×0.9	79
	14	245.773–246.710	1.6×0.9	79
	15	250.154–251.091	1.5×0.9	88
	16	251.079–252.016	1.3×0.8	86
20 January 2012	0–16	213.715–246.627	1.8×1.3	-1

2.2 Analysis

2.2.1 Reduction of SV data

With the advent of highly sensitive facilities such as ALMA, the spectral lines which were hindered by the noise level with previous telescope can now be detected. Most of these line-rich sources including hot cores are associated with detectable continuum emission. In the analysis of molecular emission lines, the determination and the subtraction of this continuum emission is an essential, but difficult task. Therefore, we improved the method devised in Sanchez-Monge et al. (2017) and deduced continuum subtraction in the observed UV domain (the raw visibilities measured by the interferometer). We introduce the method and results in this section.

Determination of the continuum level

The determination of the continuum emission level of astronomical sources observed in a spectral line observing mode is based on the identification of channels free of line emission, i.e. line-free channels.

First, we obtain the spectra for which we want to estimate the continuum level. In the case of Orion-KL, many molecular emission exist in Hot core ($\text{RA}_{J2000} : 05^{\text{h}}35^{\text{m}}14^{\text{s}}.580$, $\text{Dec}_{J2000} : -05^{\circ}22'31''.029$) or Compact ridge ($\text{RA}_{J2000} : 05^{\text{h}}35^{\text{m}}14^{\text{s}}.2775$, $\text{Dec}_{J2000} : -05^{\circ}22'30''.776$), so we extracted spectra from circular regions with a diameter of $1''$.0 with the coordinates indicated by Hirota et al. (2015) as the center. The peak of the distribution of the intensity values is determined with a Gaussian fit by assuming the Gaussian random error distribution with the mean value E and the standard deviation σ . The width is small in case of pixels with little or no line emission, but for line contaminated regions the distribution becomes broader and the exact location of the peak more uncertain. Therefore, we set the range of the Gaussian fitting from 0 to 1/3 of the peak intensity in line contaminated side, and calculated the mean value E and the standard deviation σ (see Figure 2.2.1).

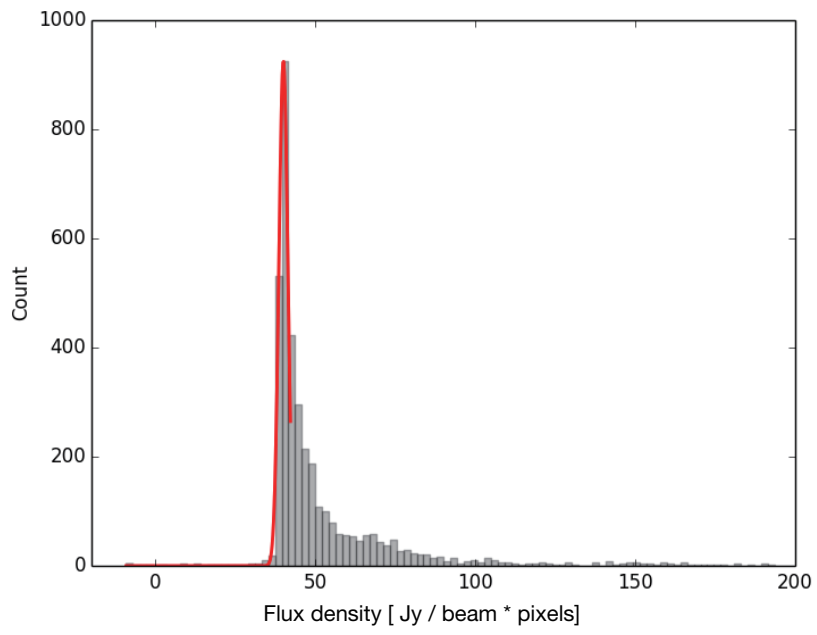


Figure 2.1: Schematic description of the process of determination of the continuum level toward Orion-KL: shown are the flux density distributions of Hot core (histogram) with the resulting fit overlaid (red line).

Imaging line cubes

Subsequently, the part of the distribution within $E - 3\sigma$ is defined as line-free channels. Hot core and Compact ridges have different spectra because of the disparate chemical composition, so we determined the line-free channels individually and subtracted the continuum in the UV domain by CASA task UVCONTSUB with channels common to the two regions. After the continuum subtraction, line cubes of Orion-KL were made using the CASA task CLEAN.

Figure 2.2 shows examples of original and continuum-subtracted spectra towards Hot core. Since the base line defined in this analysis seems to be reasonable, the continuum subtraction has succeeded.

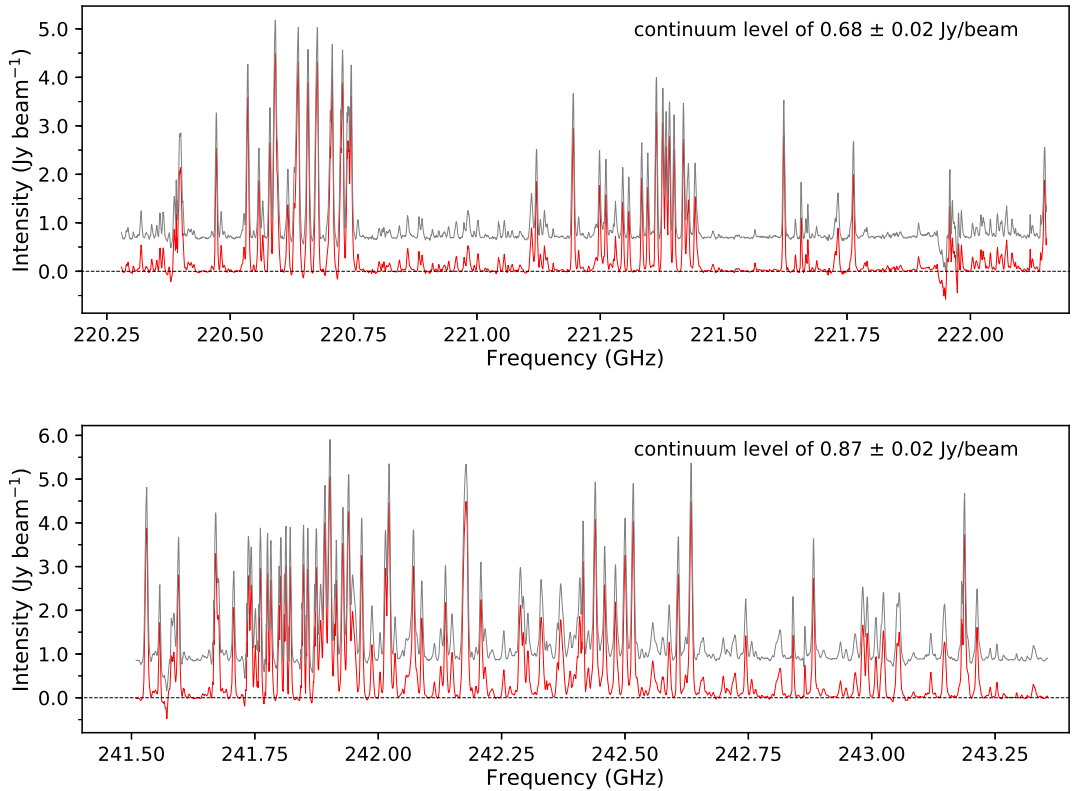


Figure 2.2: The original spectra (gray) and continuum-subtracted spectra (red) towards Hot core. The dotted line represents the base line (0 level). The continuum emission level subtracted from the original spectra, together with its uncertainty, is listed in the upper right part of each panel.

2.2.2 Line identification

In order to find out where common signals exist, we drew integrated intensity maps using CASA task IMMOMENT. The integrated velocity range is $3.0\text{-}12.0 \text{ km s}^{-1}$, corresponding to typical velocity component of Hot core ($4.8\text{-}6 \text{ km s}^{-1}$) and that of Compact ridge ($7.2\text{-}9.6 \text{ km s}^{-1}$) (Feng et al., 2015). Spectroscopic data of CH_3NH_2 are provided by Motiyenko et al. (2014) and JPL Molecular Spectroscopy catalog².

Then, since emission at the center of Hot core were found in most of integrated intensity maps, we extracted spectrum for transitions with no line blending around $\pm 2 \text{ km s}^{-1}$ from Hot core. Possible line blending (just considering the transitions $E_u < 500 \text{ K}$) with CH_3NH_2 was investigated by JPL database, the Cologne database for molecular spectroscopy (CDMS)³, and Splatalogue⁴.

Subsequently, we estimated the systemic velocity and the line width of 217.758 GHz line, which is reported by Pagani et al. (2017) and does not seem contaminated by other molecular lines by the Gaussian fitting. At last, adopting the systemic velocity and the line width of the 217.758 GHz line to other transitions, we obtained the integrated intensity of 6 transitions described in Table 3.1.

²<http://spec.jpl.nasa.gov>

³<http://www.astro.uni-koeln.de/cdms/>

⁴<http://www.splatalogue.net/>

Chapter 3

Results

The data obtained for CH₃NH₂ are summarized in Table 3.1. Here the rest frequencies, $S\mu^2$, the upper state energy (E_u), the quantum numbers, the peak brightness temperature, the systemic velocity (V_{LSR}), and noise level are listed. Out of 32 predicted transitions ($S\mu^2 > 25 \text{ D}^2$ and $E_u < 200 \text{ K}$) in our observational frequency range, 6 were probably identified in this data set, and are reported in Table 3.1. The remaining 18 CH₃NH₂ transitions are blended with or masked by other spectral features, or its signal are below the noise level (See Appendix B).

Table 3.1: Observed rotational transitions of CH₃NH₂ in Orion-KL

Frequency [GHz]	$S\mu^2 [\text{D}^2]$	$E_u [\text{K}]$	Transition (J, K_a, Γ)	Noise [K]	Comments
217.758	129.88	182.05	12, 2, $B_2 \rightarrow 12, 1, B_1$	0.034	Reported in Pagani+17
245.202	37.84	168.31	12, 1, $B_2 \rightarrow 11, 2, B_1$	0.037	Reported in Pagani+17
229.908	27.37	92.71	8, 2, $A_2 \rightarrow 8, 1, A_1$	0.064	
235.735	82.06	92.76	8, 2, $B_2 \rightarrow 8, 1, B_1$	0.081	Reported in Pagani+17
242.262	60.23	60.86	6, 2, $B_2 \rightarrow 6, 1, B_1$	0.166	SV data
244.887	49.54	48.09	5, 2, $B_1 \rightarrow 5, 1, B_2$	0.043	Reported in Pagani+17

3.1 Overall CH₃NH₂ distribution

CH₃NH₂ emission appears mainly at Hot core and partially at IRc7. According to previous work (see e.g., Feng et al., 2015; Gong et al., 2015), N-bearing species tend to have

similar peak at or near Hot core. CH_3NH_2 also shows the same trend.

In the integrated intensity map of 229.908 GHz line, emission come from the south part of Hot core. Since it can be confirmed that the velocity component is different in the channel map (see Figure 3.7), this is considered to be the emission of another molecular line.

In addition, the extended emission in Hot core and the compact structure at Compact ridge are seen in the integrated intensity map of 242.262 GHz line. These are also considered to be emission from other molecule line by the channel map (Figure 3.6) and spectrum (Figure 3.2).

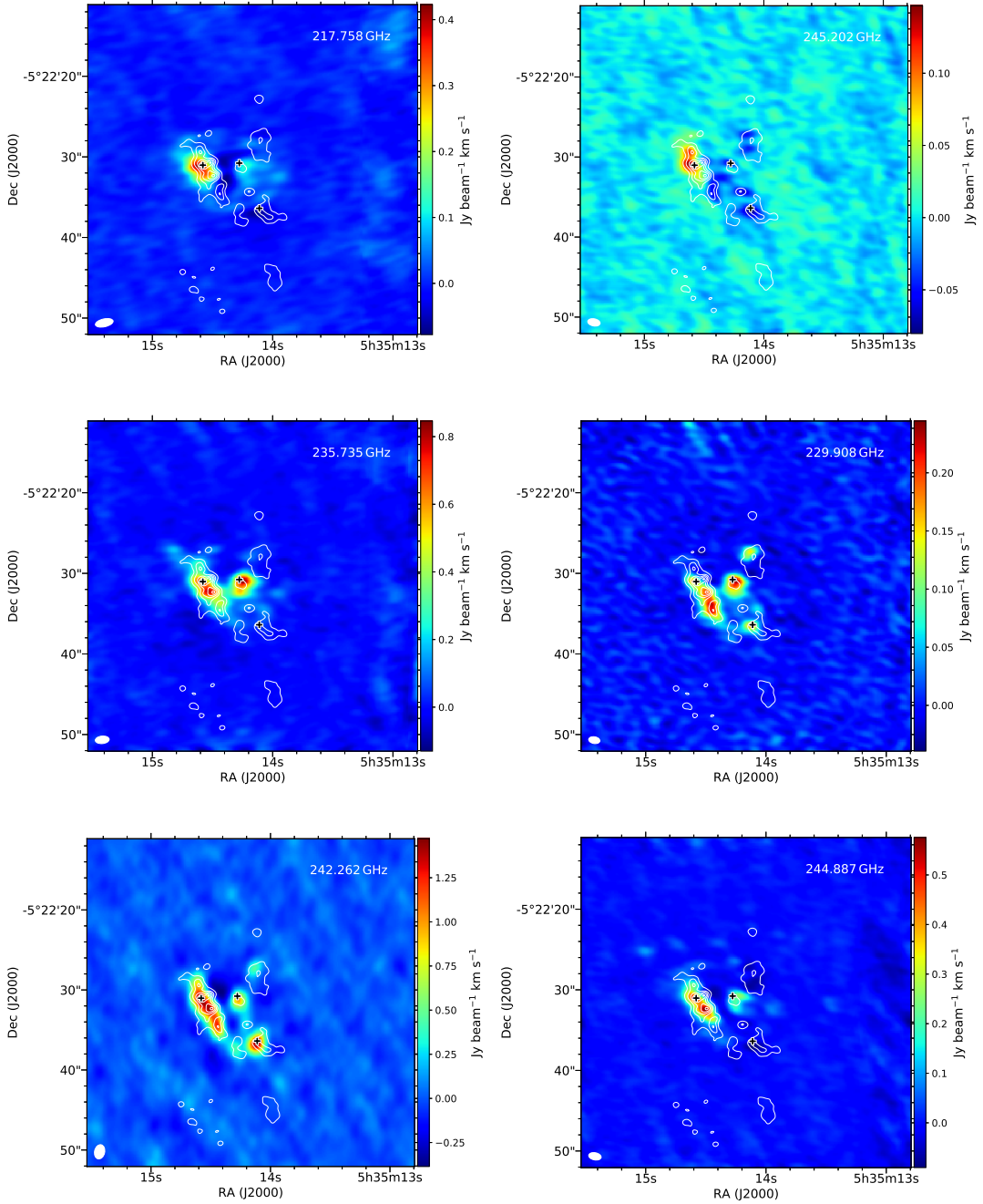


Figure 3.1: Integrated intensity maps of unblended CH_3NH_2 lines. The white contours show the 1.3 mm continuum map from Hirota et al. (2015), where the contour levels are 10 %, 30 %, 50 %, 70 %, 90 % of the peak intensity. Black crosses denote Hot core, IRc7, and Compact ridge. The rest frequency of each transition shows in the upper right part of each panel.

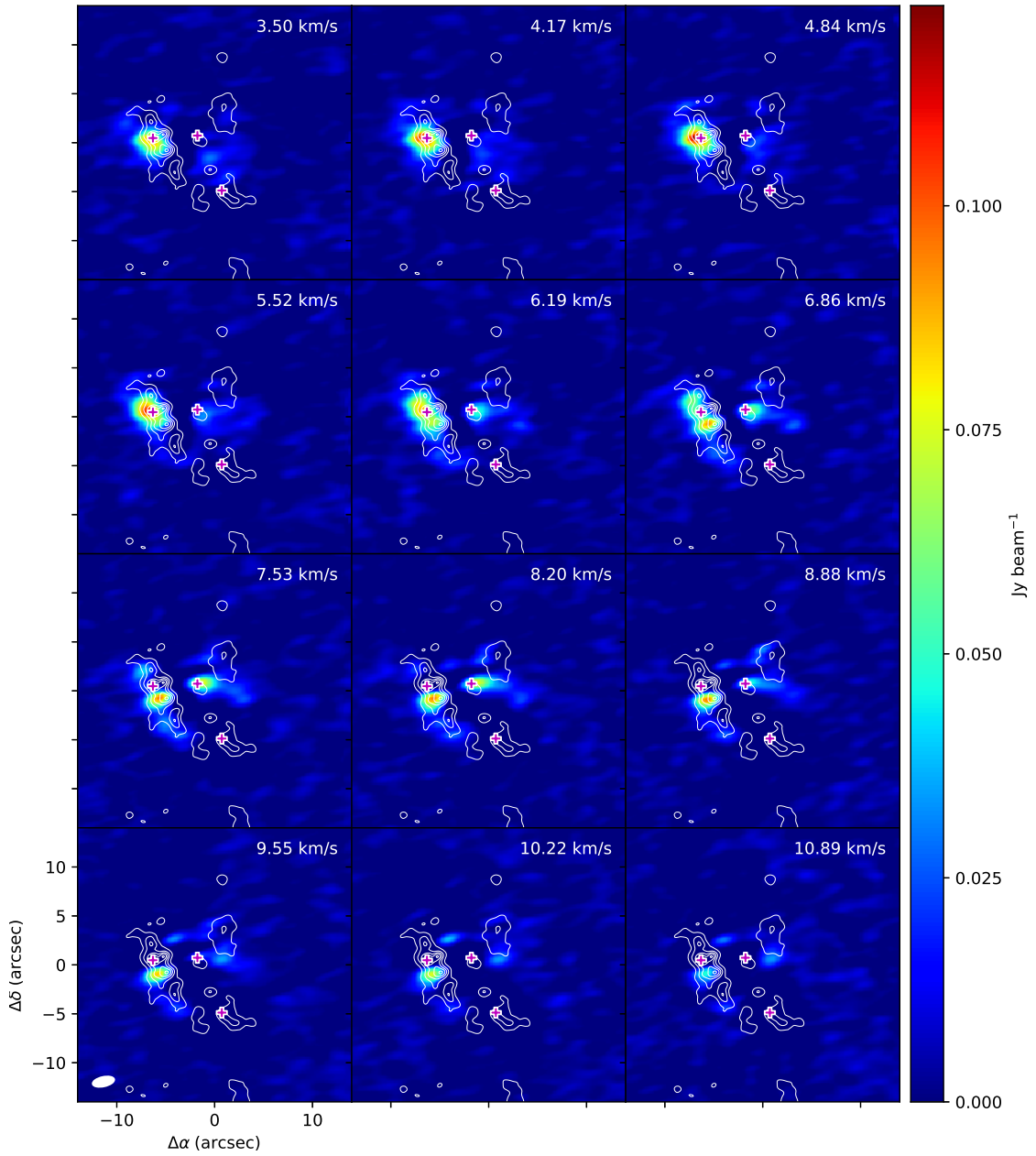


Figure 3.2: Channel map of expected unblended 217.758 GHz line show multiple velocity-dependent emission peaks: $4\text{-}6 \text{ km s}^{-1}$ towards Hot core, $7\text{-}9 \text{ km s}^{-1}$ towards IRc7. Magenta crosses denote Hot core, IRc7, and Compact ridge.

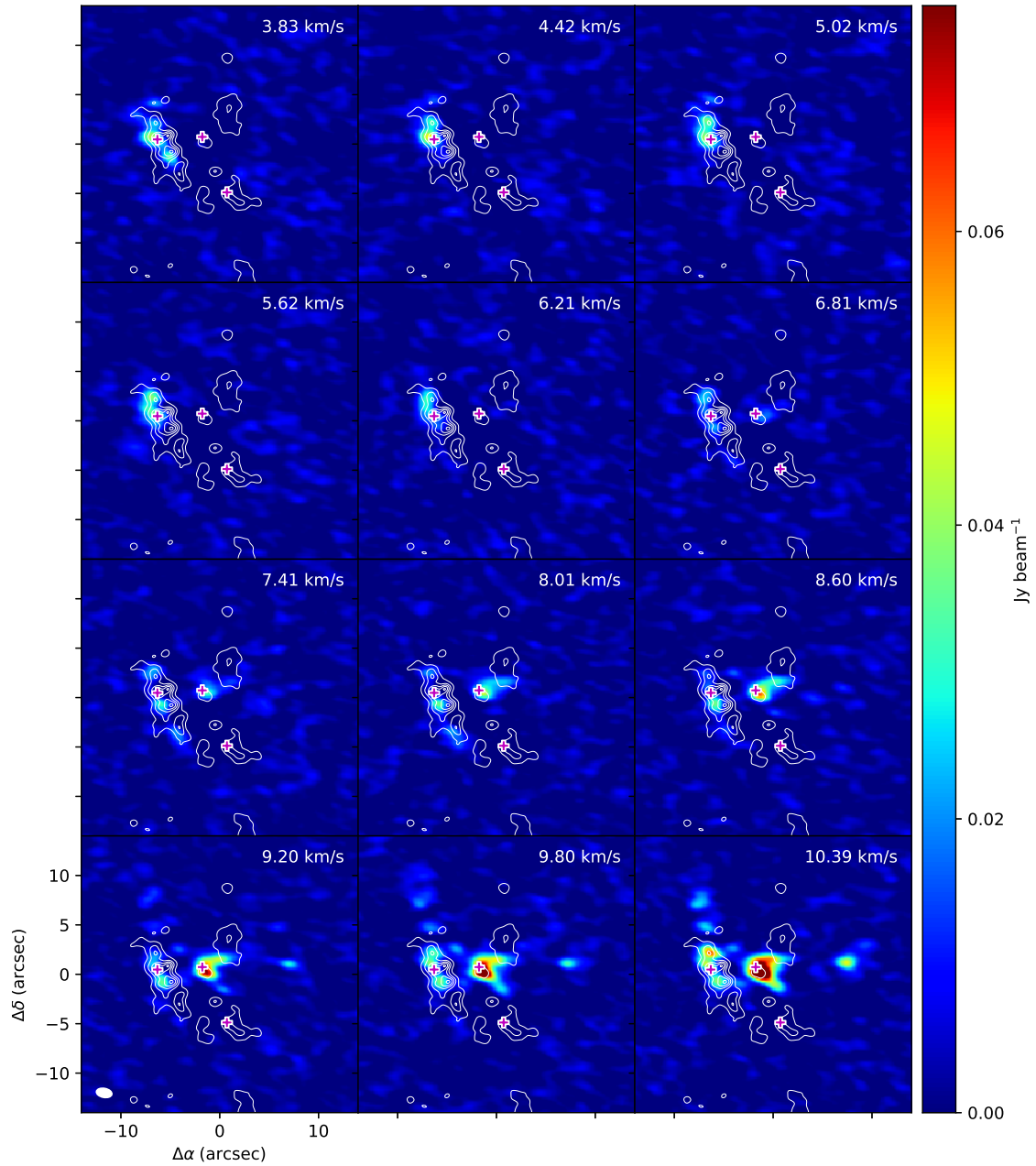


Figure 3.3: Channel map of expected unblended 245.202 GHz line.

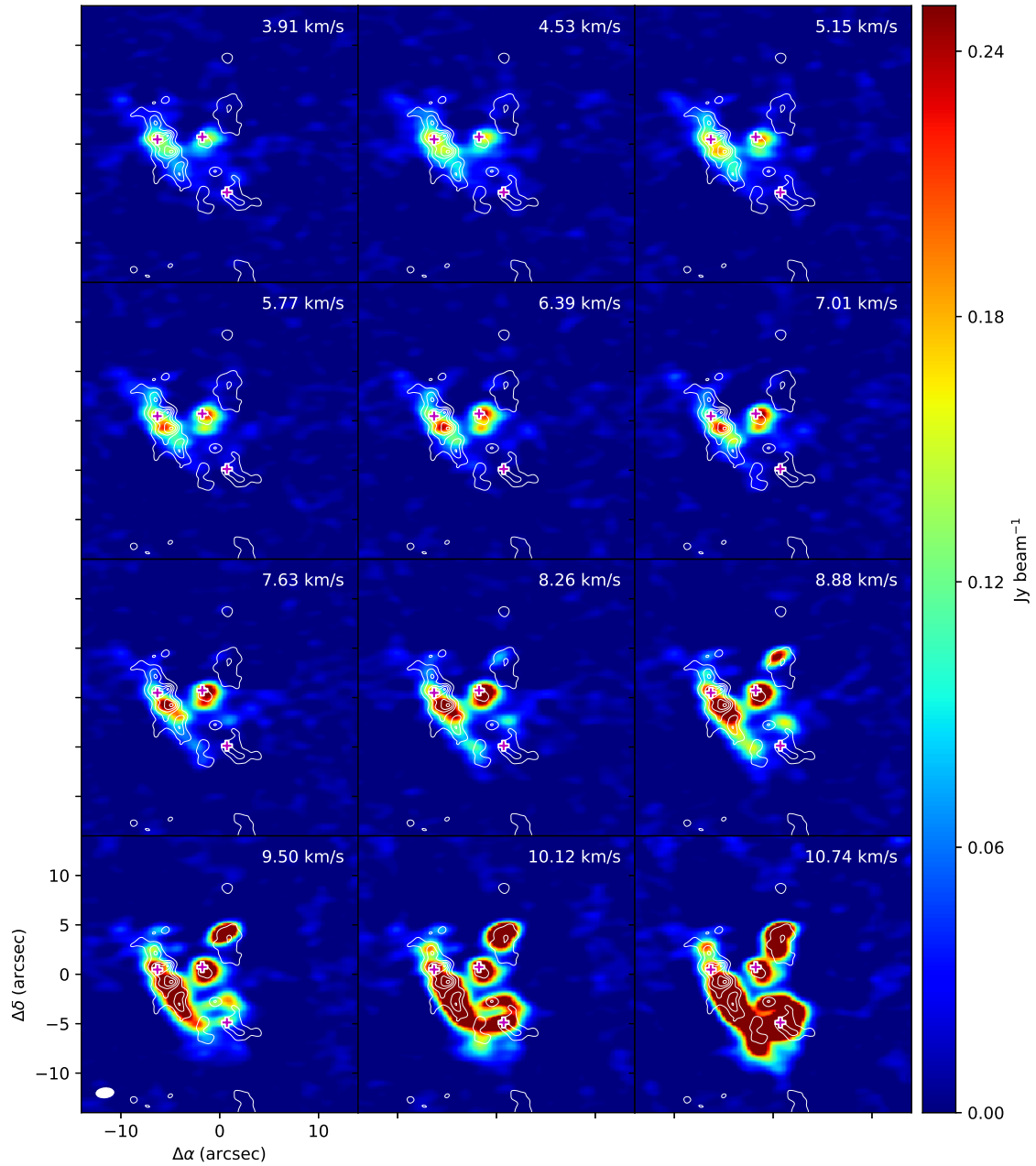


Figure 3.4: Channel map of expected unblended 235.735 GHz line.

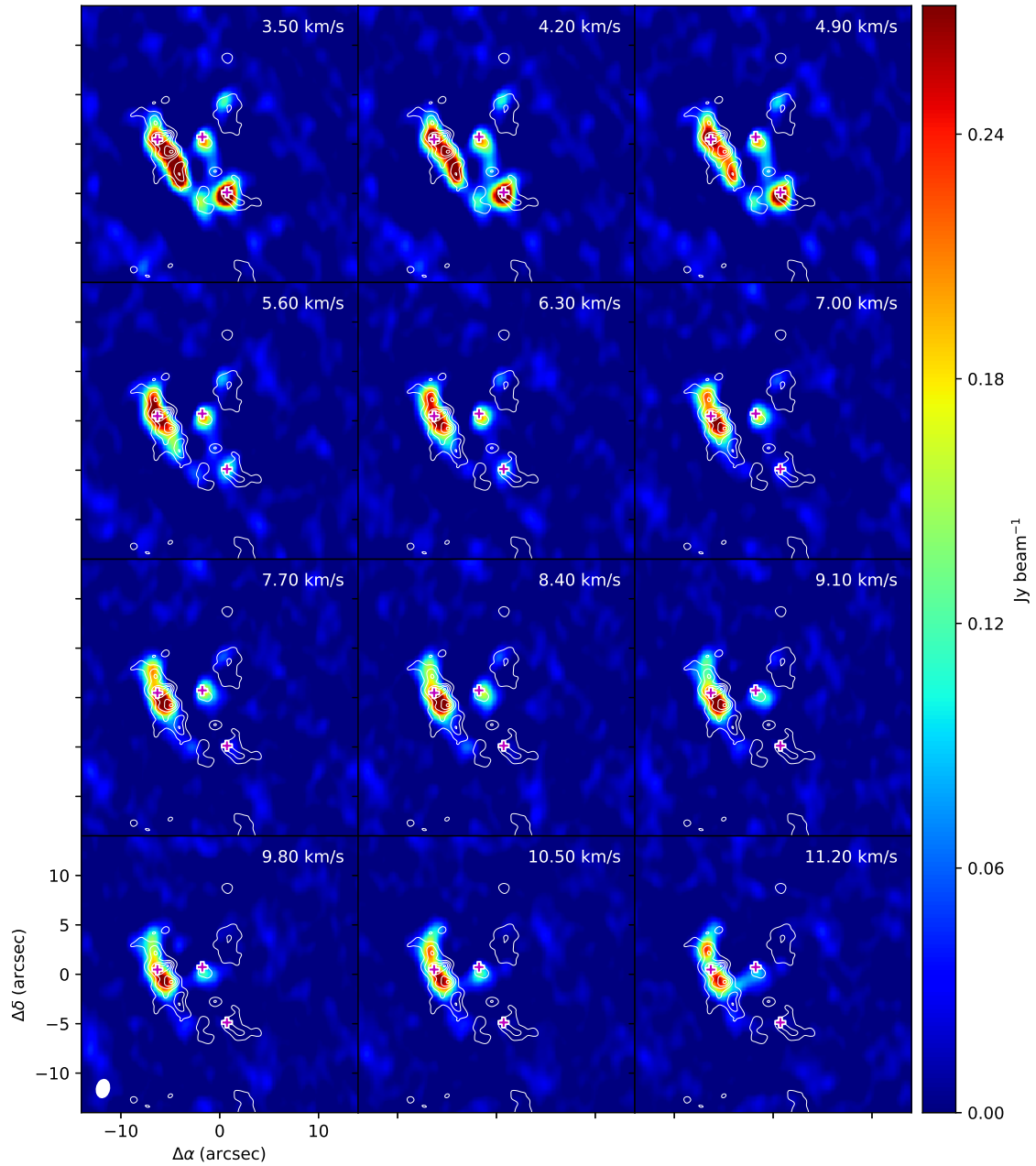


Figure 3.5: Channel map of expected unblended 242.262 GHz line.

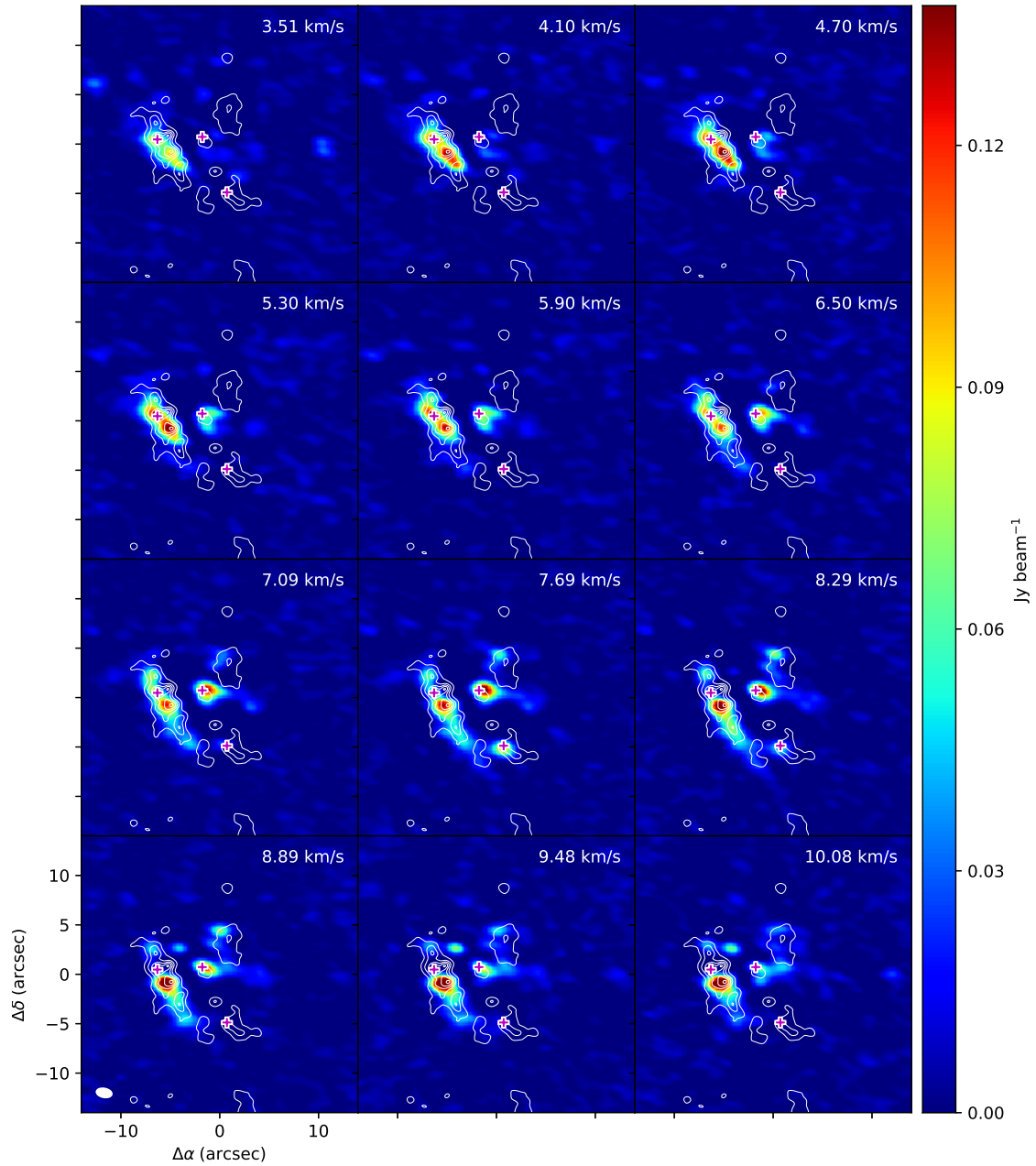


Figure 3.6: Channel map of expected unblended 244.887 GHz line.

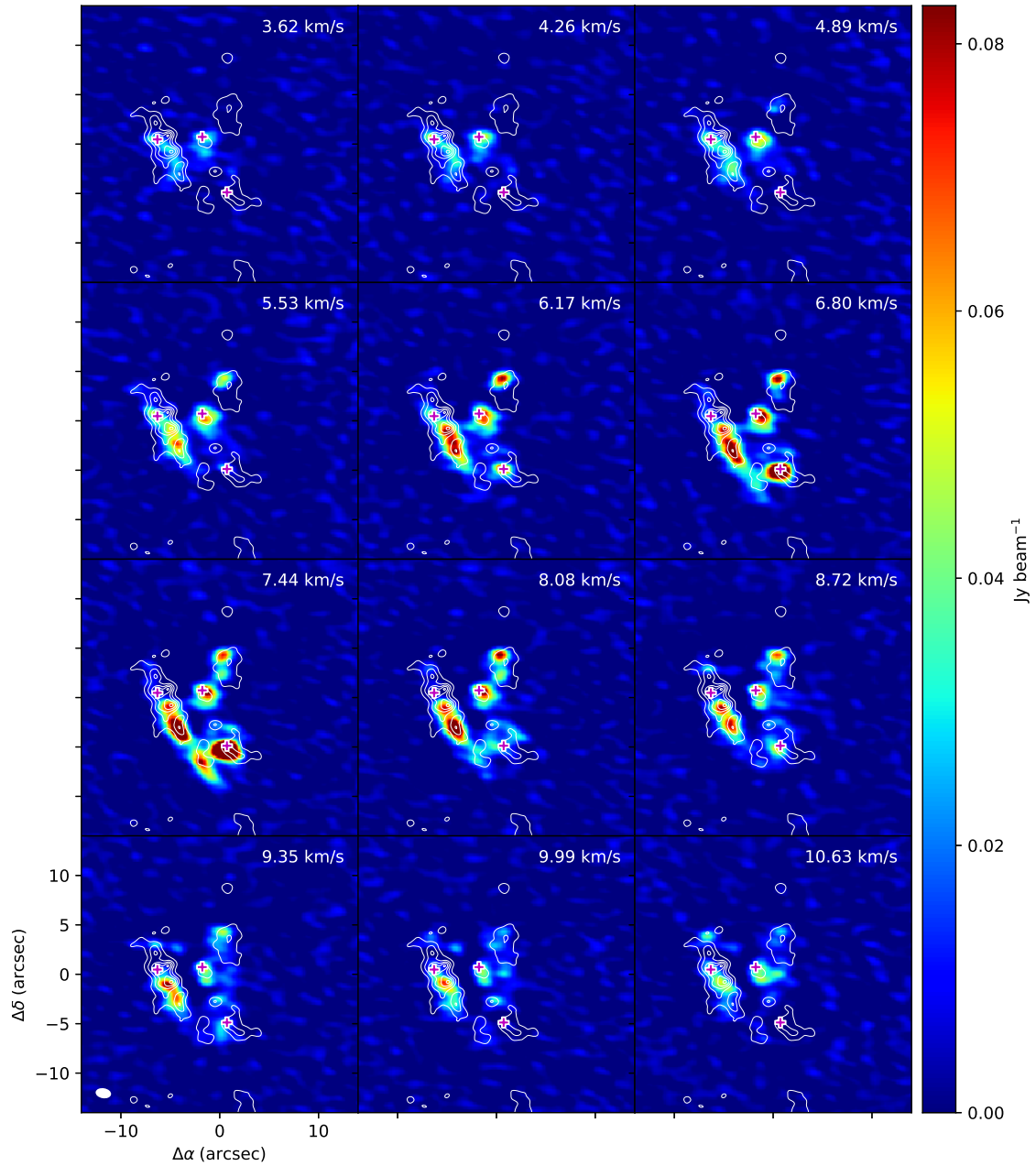


Figure 3.7: Channel map of expected unblended 229.908 GHz line.

3.2 Spectrum

The spectrum were extracted from the region of $1''.0$ in diameter around Hot core ($\text{RA}_{J2000} : 05^{\text{h}}35^{\text{m}}14^{\text{s}}.580$, $\text{Dec}_{J2000} : -05^{\circ}22'31''.029$), and the Gaussian fitting was performed to obtain FWHM line widths and the mean local standard of rest velocity V_{LSR} of the emission lines. The line measurements toward Hot core are listed in Table 3.2.

The average LSR velocity and FWHM line width are estimated to be $4.84 \pm 0.22 \text{ km s}^{-1}$ and $4.16 \pm 0.79 \text{ km s}^{-1}$, respectively. V_{LSR} are consistent with those reported by Feng et al. (2015) for N-bearing COMs observed toward the Hot core (e.g, 4.9 km s^{-1} for CH_2CHCN , 5.1 km s^{-1} for $\text{CH}_3\text{CH}_2\text{CN}$). On the other hand, $\Delta V_{1/2}$ of CH_3NH_2 is narrower than those of other molecule in Hot core (typically $5\text{--}15 \text{ km s}^{-1}$, Pagani et al., 2017).

Table 3.2: CH_3NH_2 line parameters toward Hot core

Frequency [GHz]	E_u [K]	peak T_B [K]	V_{LSR} [km s^{-1}]	$\Delta V_{1/2}$ [km s^{-1}]	Noise [K]	Note
217.758	182.05	0.86(0.03)	4.73(0.08)	3.99(0.24)	0.034	
245.202	168.31	0.37(0.01)	4.51(0.08)	3.86(0.33)	0.037	
229.908	92.71	0.65(0.01)	4.91(0.03)	3.19(0.06)	0.064	
235.735	92.76	1.70(0.02)	4.86(0.03)	5.60(0.10)	0.081	
242.262	60.86	2.03(0.03)	4.80(0.09)	8.04(0.23)	0.166	Partially blended
244.887	48.09	1.29(0.57)	5.23(0.90)	4.16(2.12)	0.043	

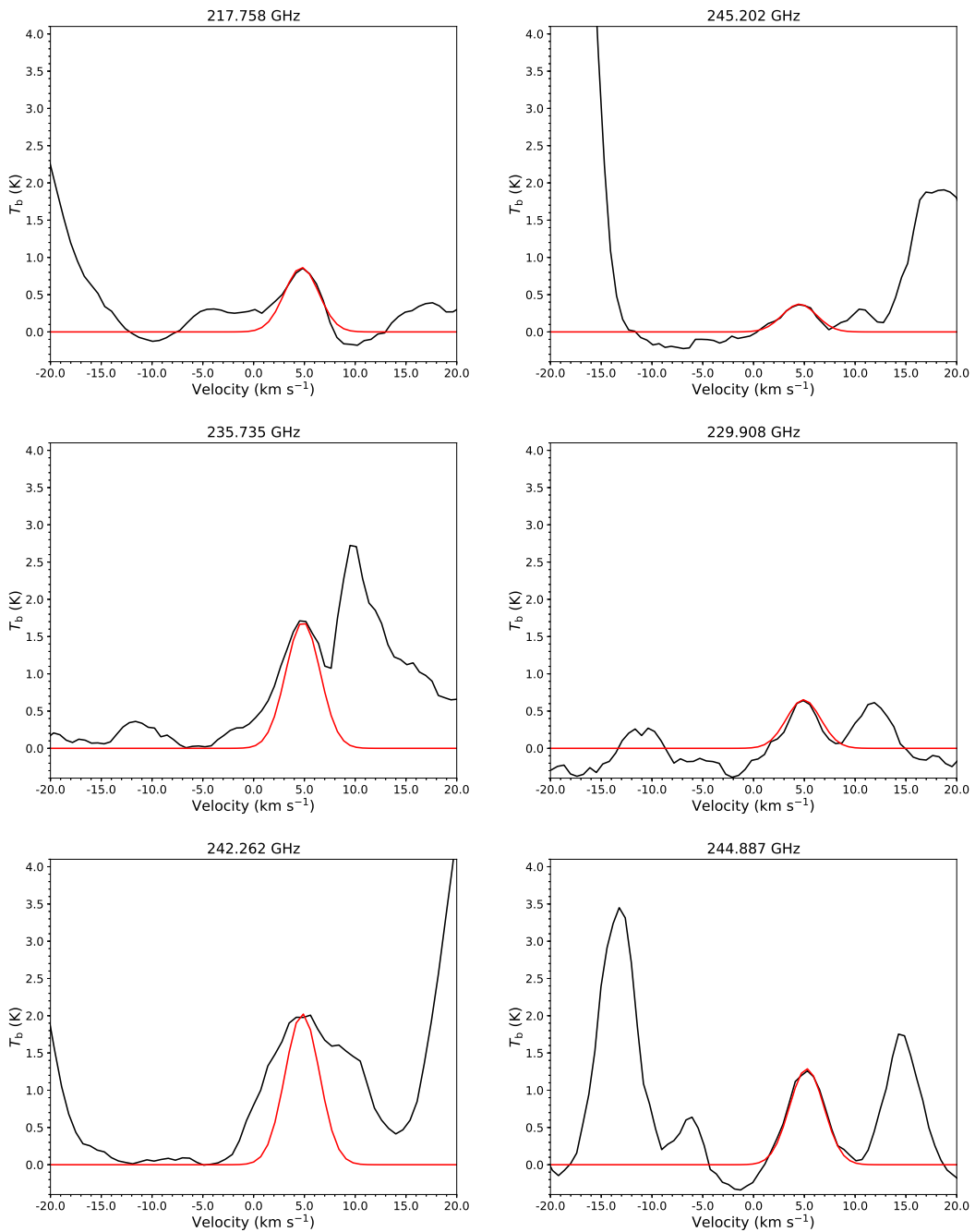


Figure 3.8: Spectrum of the CH_3NH_2 lines at each frequency observed in Hot core center (black) and the result of the Gaussian fitting assuming the average $\Delta V_{1/2} = 4.2 \text{ km s}^{-1}$ (red).

Chapter 4

Discussion

4.1 Column density and Rotation temperature

In this subsection we will describe the methodologies in deriving the column density and the rotational temperature of COMs. The column density of CH₃NH₂ (N_{MA}) was estimated by using the rotational temperature diagram method, which assumes local thermodynamic equilibrium (LTE) and optically thin emission. The following equation was employed for the analysis (Turner, 1991):

$$\log \frac{3 k_{\text{B}} T_{\text{B}} \Delta V_{1/2}}{8 \pi^3 \nu S \mu_0^2} = \log \frac{N_{\text{MA}}}{U_{\text{rot}}} - \frac{E_{\text{u}} \log e}{k_{\text{B}} T_{\text{rot}}} \quad (4.1)$$

In the expression, ν is the rest frequency of the transition, μ_0 is the permanent dipole moment, U_{rot} is the rotational partition function, S is the line strength, E_{u} is the upper state energy, and T_{B} and $\Delta V_{1/2}$ are the brightness temperature and line widths (FWHM, in km s⁻¹), respectively. We assumed the average $\Delta V_{1/2} = 4.2$ km s⁻¹, which derived by the Gaussian fitting.

The brightness temperature can be converted from intensity I_{ν} when the Rayleigh-

Jeans law is applicable.

$$T_B = \frac{c^2}{2 k_B \nu^2} I_\nu \quad (4.2)$$

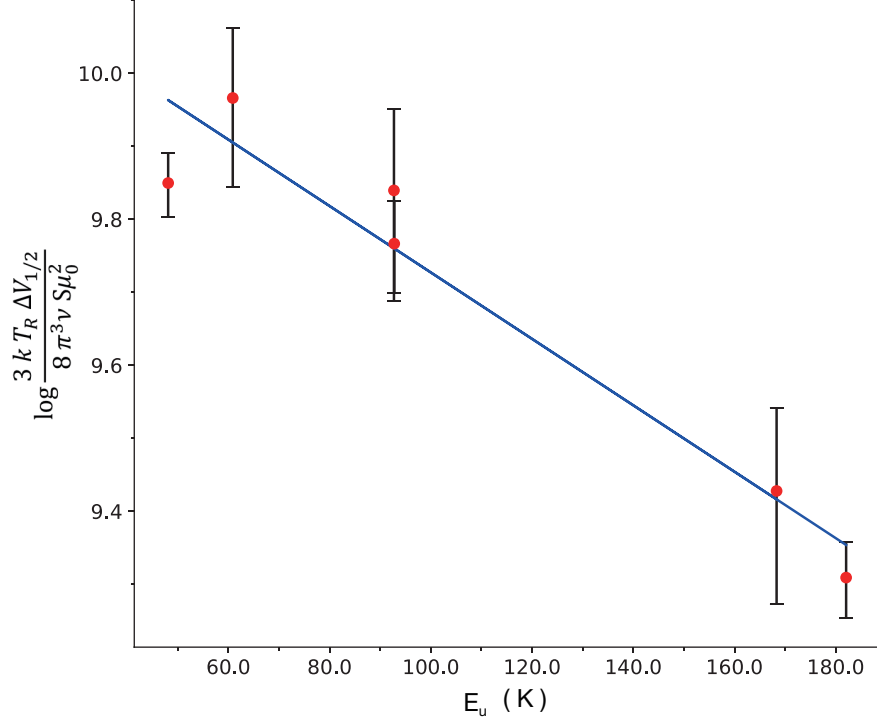


Figure 4.1: Rotation diagram of CH_3NH_2 in Hot core. The error bars represents $\pm 3 \sigma$ for each data.

The resulting plots are given in Figure 4.1. The analysis yields a rotational temperature of $T_{\text{rot}} = 95.4^{+15.5}_{-11.7}$ K, with a column density of $N_{\text{MA}} = (5.5^{+1.6}_{-1.1}) \times 10^{14} \text{ cm}^{-2}$.

4.2 Suspicious lines

Comparison of catalogs did not suggest contamination, but some emission lines could not be detected as CH_3NH_2 .

As shown in Figure 4.2, the CH_3NH_2 data including 2 transitions in Table 4.1 produced point-to-point scatter perhaps because of the lower signal-to-noise ratio for the

Table 4.1: transitions of CH_3NH_2

Frequency [GHz]	$S\mu^2$ [D^2]	E_u [K]	Transition (J, K_a, Γ)	peak T_B [K]	V_{LSR} [km s^{-1}]	Noise [K]	Comments
215.670	53.92	111.48	9, 2, $E_{1-1} \rightarrow 9, 1, E_{1+1}$	3.74(0.07)	5.37(0.07)	0.043	
221.755	35.06	133.11	10, 2, $A_2 \rightarrow 10, 1, A_1$	0.33(0.03)	5.35(0.19)	0.133	SV data

weaker transitions in SV data and possible high-level contamination.

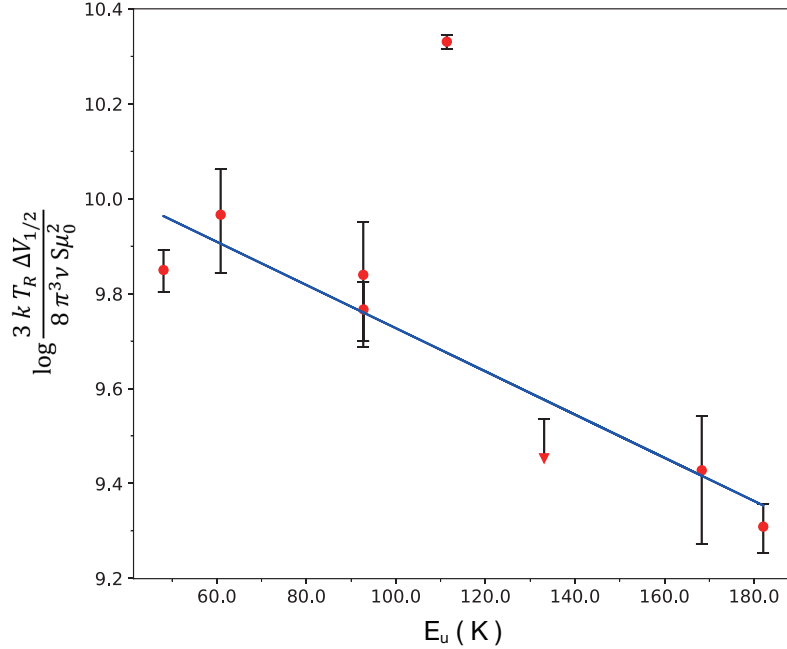


Figure 4.2: Rotation diagram of CH_3NH_2 in Hot core with additional 2 lines. The error bars on round plots represents $\pm 3\sigma$ for each data. A signal below 3σ is represented by a triangle with the error bar indicating the upper limit. The blue line is the same one as Figure 4.1.

215.670 GHz line

This emission line ($E_u = 111$ K) is seen at Hot core and IRc7 like other CH_3NH_2 transitions (see Figure 4.2), but this line has stronger intensity than that predicted in the rotation diagram. Since the line width is also wider than the other CH_3NH_2 transitions, it appears that this line is blended with other molecular emission lines existing in Hot core. Then examining the catalog including the transition of higher excitation, $\text{CH}_3\text{CH}_2\text{CN}$ (215.6687 GHz, $E_l = 604.845$ K) has come up as a candidate for blending. However, considering

that T_{rot} of $\text{CH}_3\text{CH}_2\text{CN}$ in Hot core is 155 K (Feng et al., 2015), it is uncertain how much this transition of higher excitation contributes to the blending.

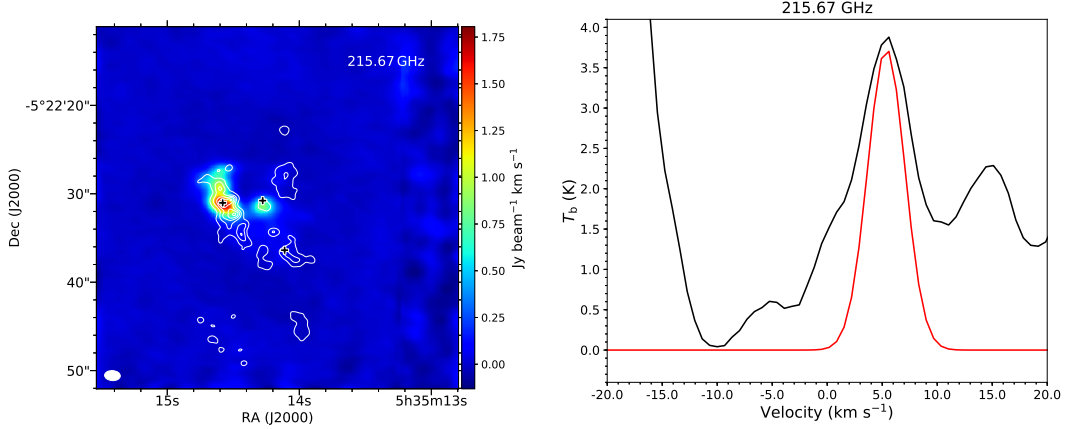


Figure 4.3: (left) Integrated intensity map of the emission for 215.670 GHz. (right) Spectrum of the CH_3NH_2 lines at each frequency observed in Hot core center (black) and the result of the Gaussian fitting assuming the average $\Delta V_{1/2} = 4.2 \text{ km s}^{-1}$ (red)

221.755 GHz line

A faint signal was seen in the center of the hot core in the integrated intensity map (Figure 4.2). Since there was no blend of other molecular emission lines in the comparison in the catalogs, we analyzed the spectrum, but the peak intensity ($T_B = 0.33 \text{ K}$) was weaker than 3σ noise level ($T_B = 0.133 \text{ K}$, see Table 4.1). When we plotted this line on the rotation diagram with 3σ as the upper limit of the intensity, the derived value was consistent with other CH_3NH_2 transitions. This emission line was included in SV data cube, so it could be possible to detect the line in future observations with higher S/N ratio.

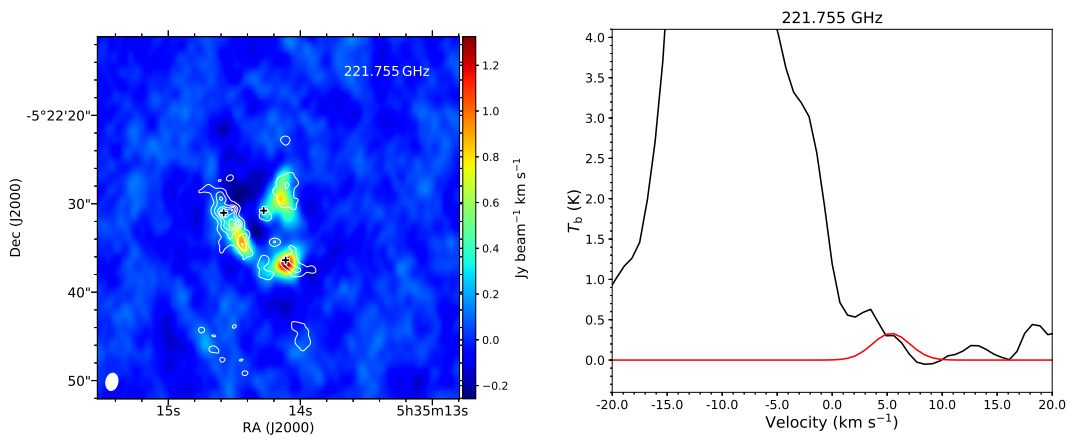


Figure 4.4: (left) Integrated intensity map of the emission for 221.755 GHz. (right) Spectrum of the CH_3NH_2 lines at each frequency observed in Hot core center (black) and the result of the Gaussian fitting assuming the average $\Delta V_{1/2} = 4.2 \text{ km s}^{-1}$ (red)

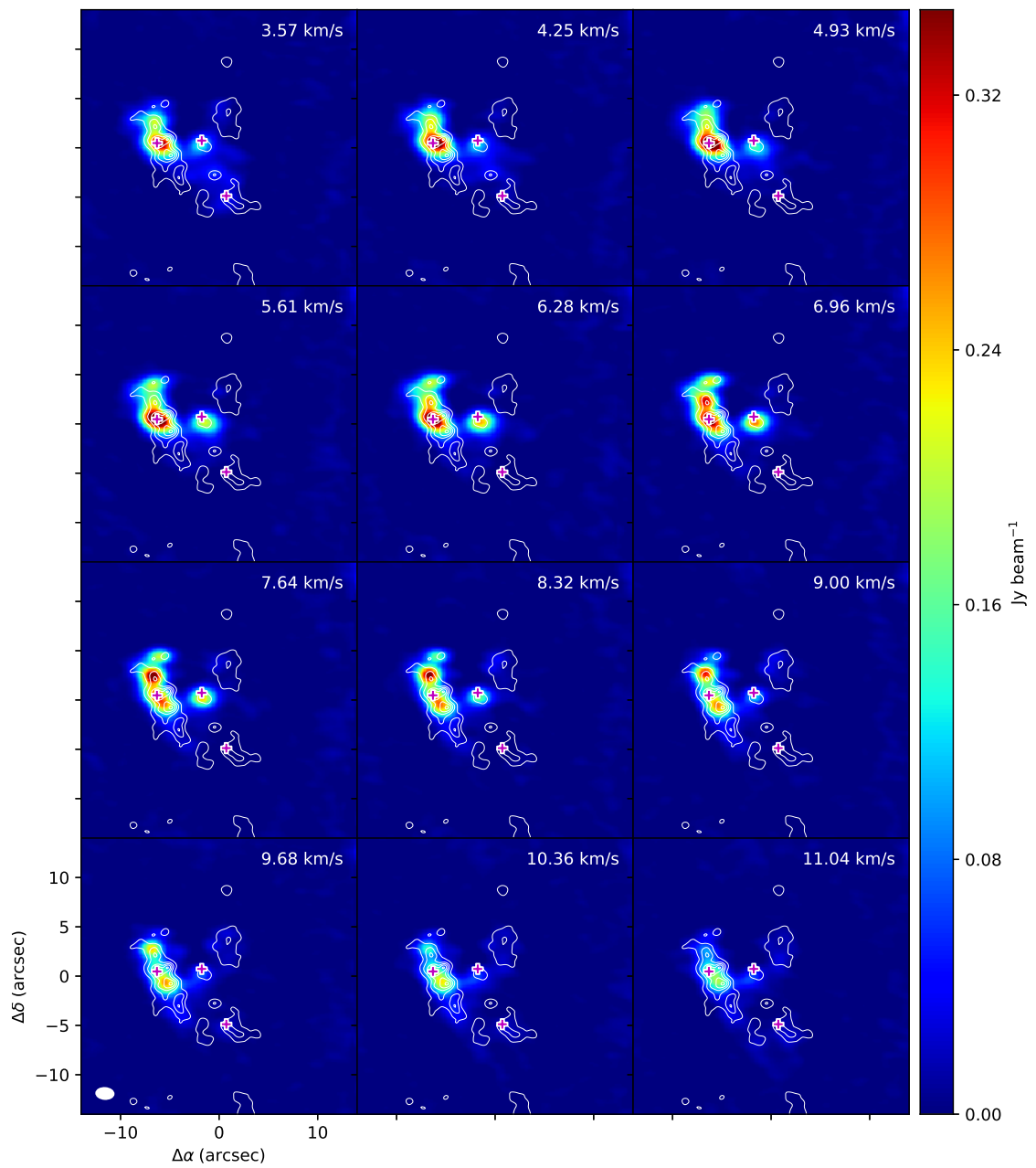


Figure 4.5: Channel map around 215.670 GHz.

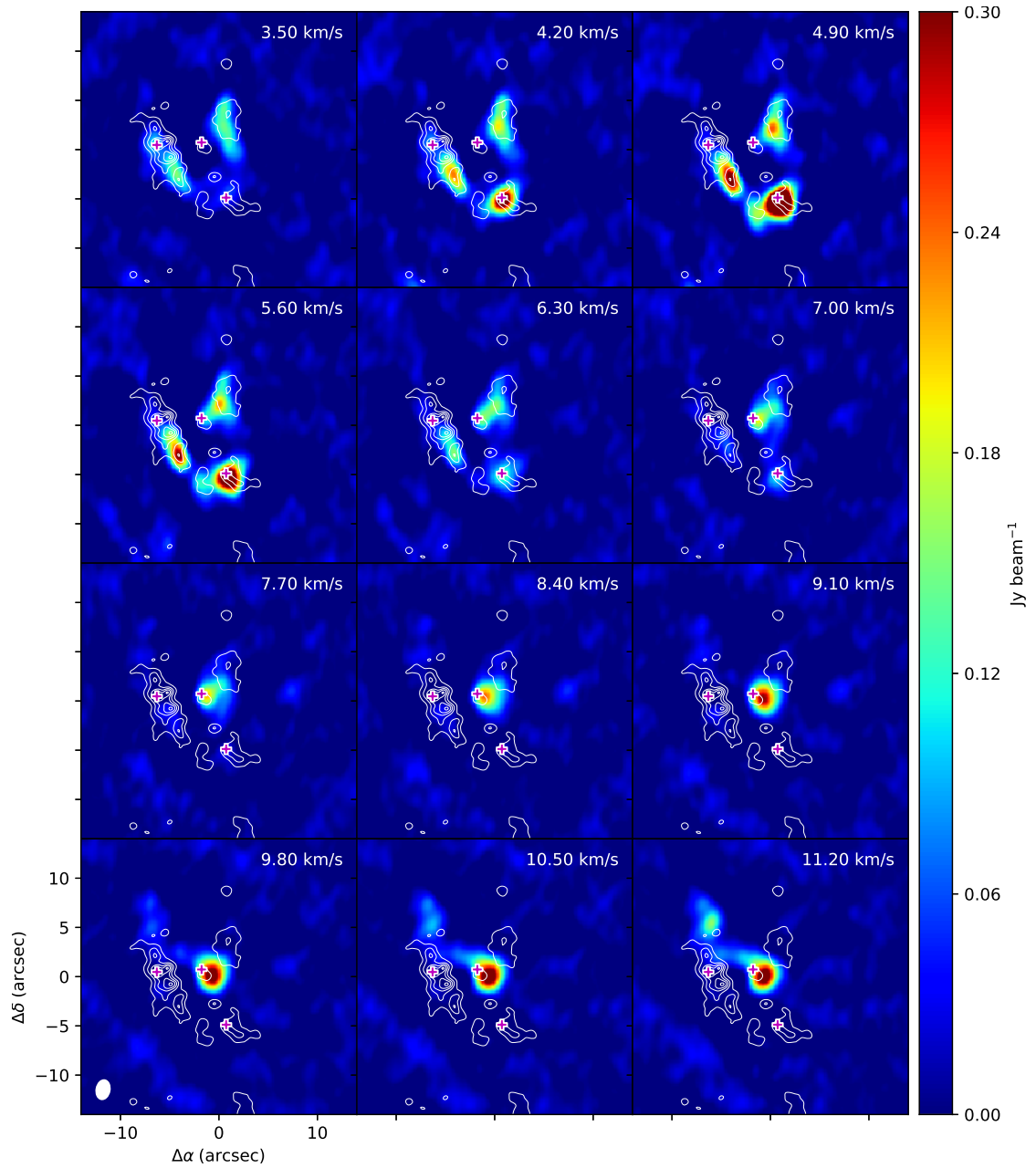


Figure 4.6: Channel map around 221.755 GHz line.

Chapter 5

Conclusions

Appendix A

Methylamine survey in low mass star-forming regions

A.1 IRAS 16293

A.1.1 Observation data

A.1.2 Results

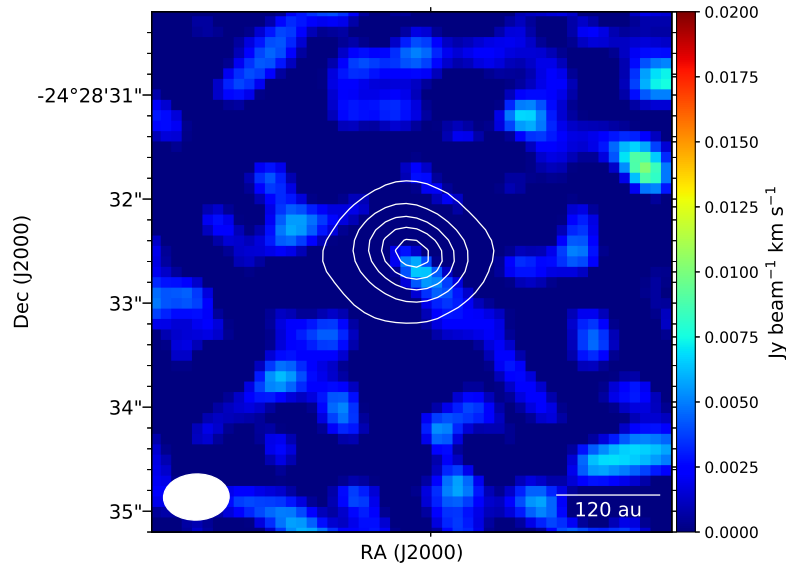


Figure A.1: Integrated intensity map around 247.362 GHz. The white contours represent the 1.3 mm continuum map, where the contour levels are 10 %, 30 %, 50 %, 70 %, 90 % of the peak intensity.

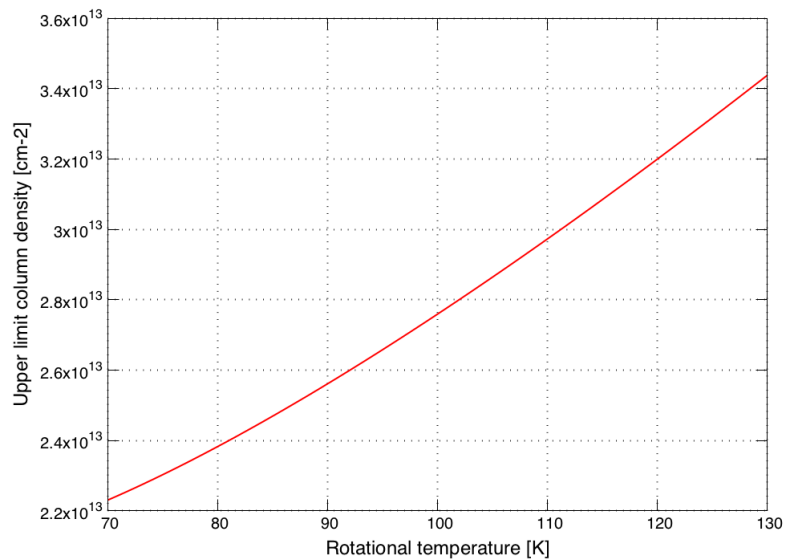


Figure A.2: Upper limit column density for the strongest CH₃NH₂ transition ($7_2E_{1-1} \rightarrow 7_1E_{1-1}$) as function of T_{rot}. A 3σ value of 11.4 mJy beam⁻¹ is used.

A.2 L483

A.2.1 Observation data

A.2.2 Results

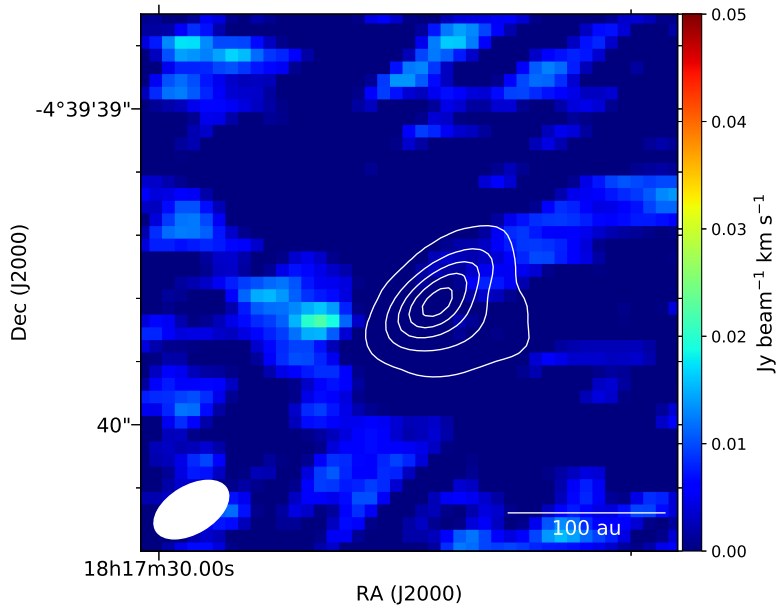


Figure A.3: Integrated intensity map around 217.079 GHz. The white contours represent the 1.3 mm continuum map, where the contour levels are 10 %, 30 %, 50 %, 70 %, 90 % of the peak intensity.

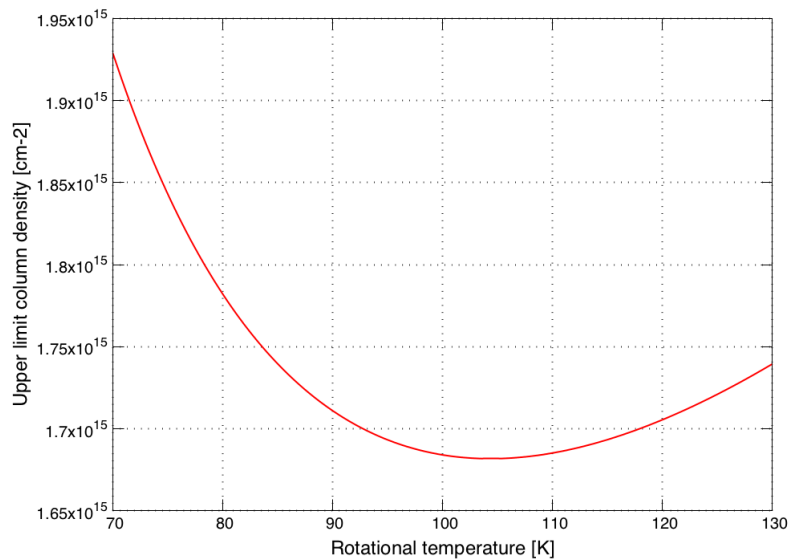


Figure A.4: Upper limit column density for the strongest CH_3NH_2 transition ($11_2A_1 \rightarrow 11_2A_2$) as function of T_{rot} . A 3σ value of $22.5 \text{ mJy beam}^{-1}$ is used.

Appendix B

Distribution of methylamine lines contaminated by other molecular line emission in Orion-KL

B.1 Integrated intensity maps

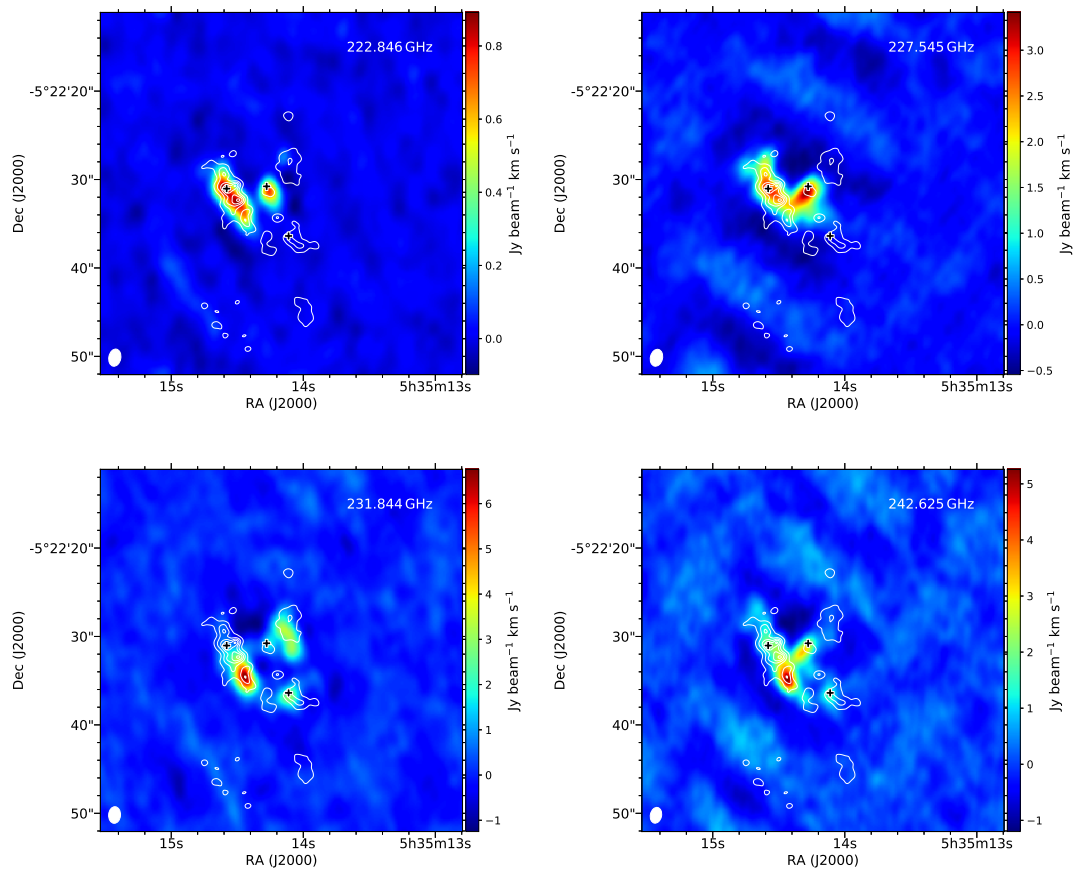


Figure B.1: Integrated intensity maps around methylamine line.

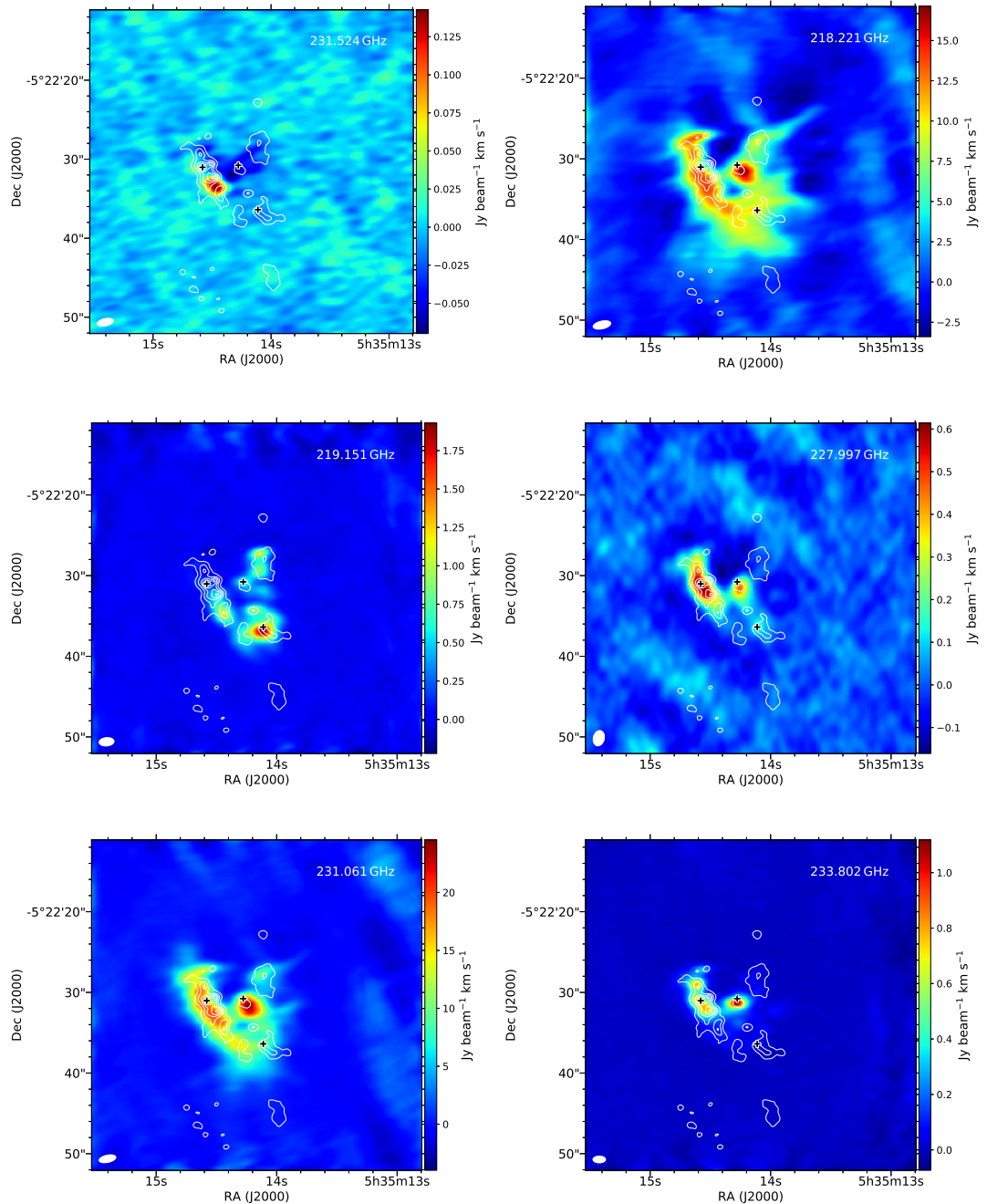


Figure B.2: (Continued)

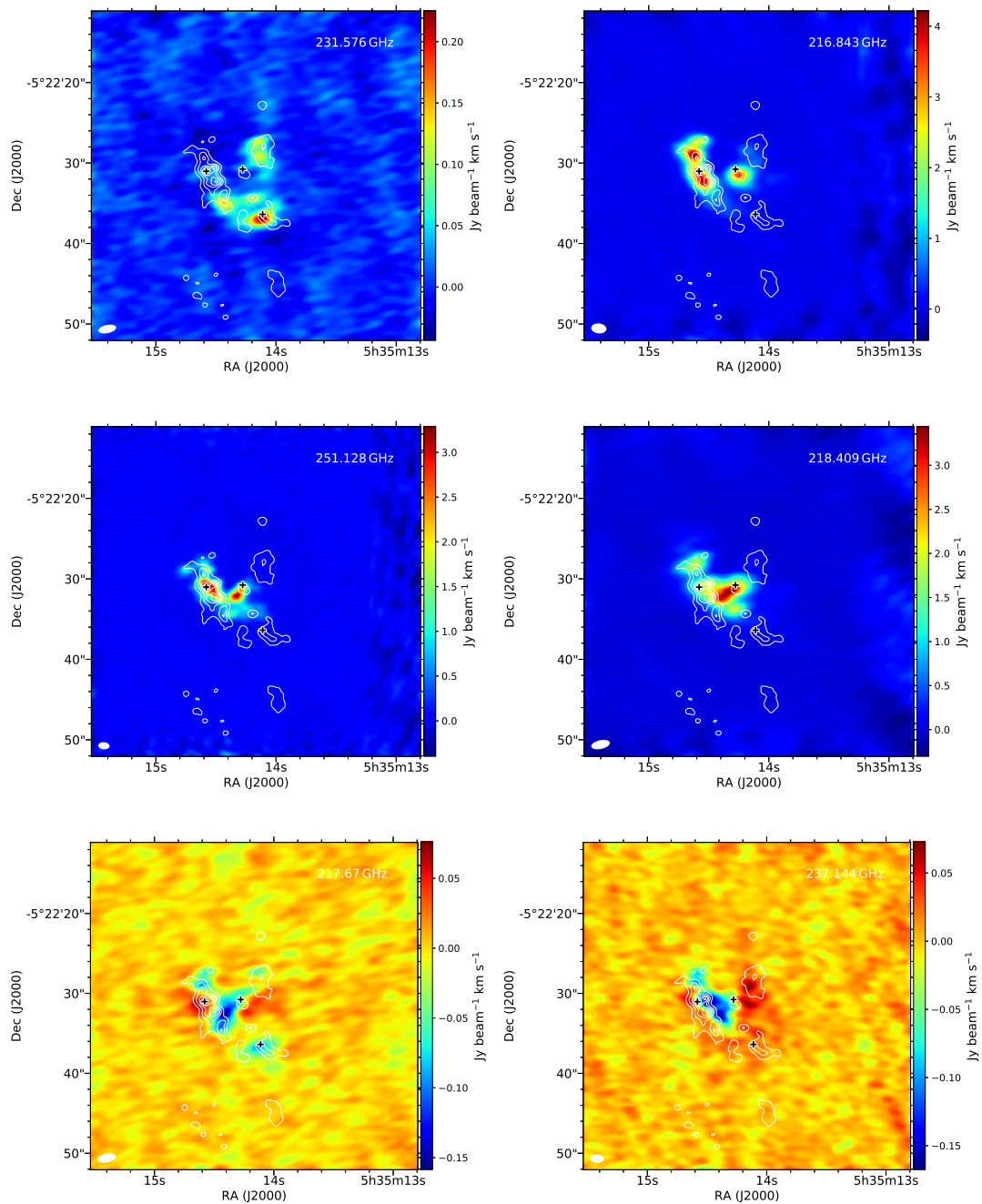


Figure B.3: (Continued)

B.2 Channel maps

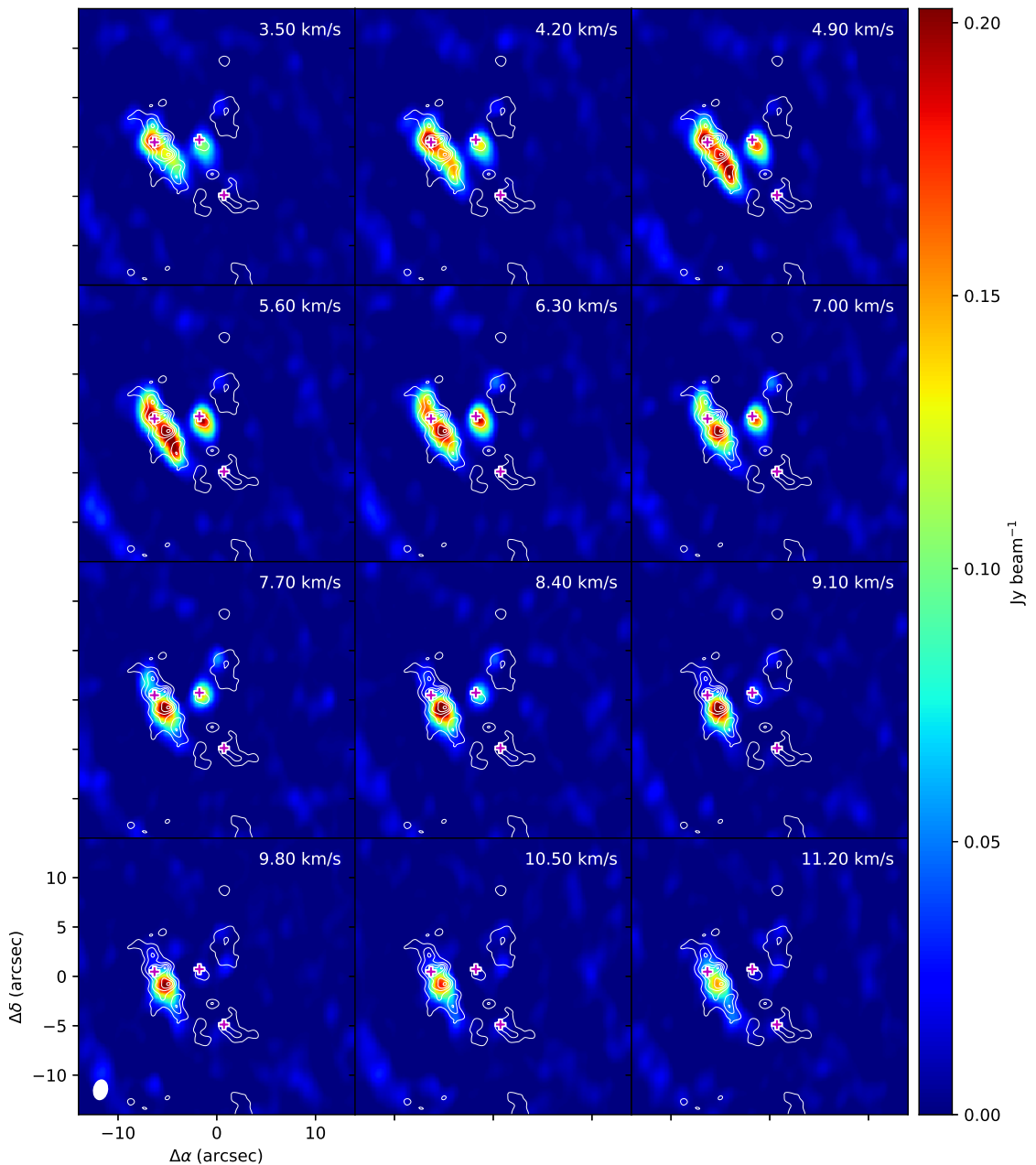


Figure B.4: 222.846GHz

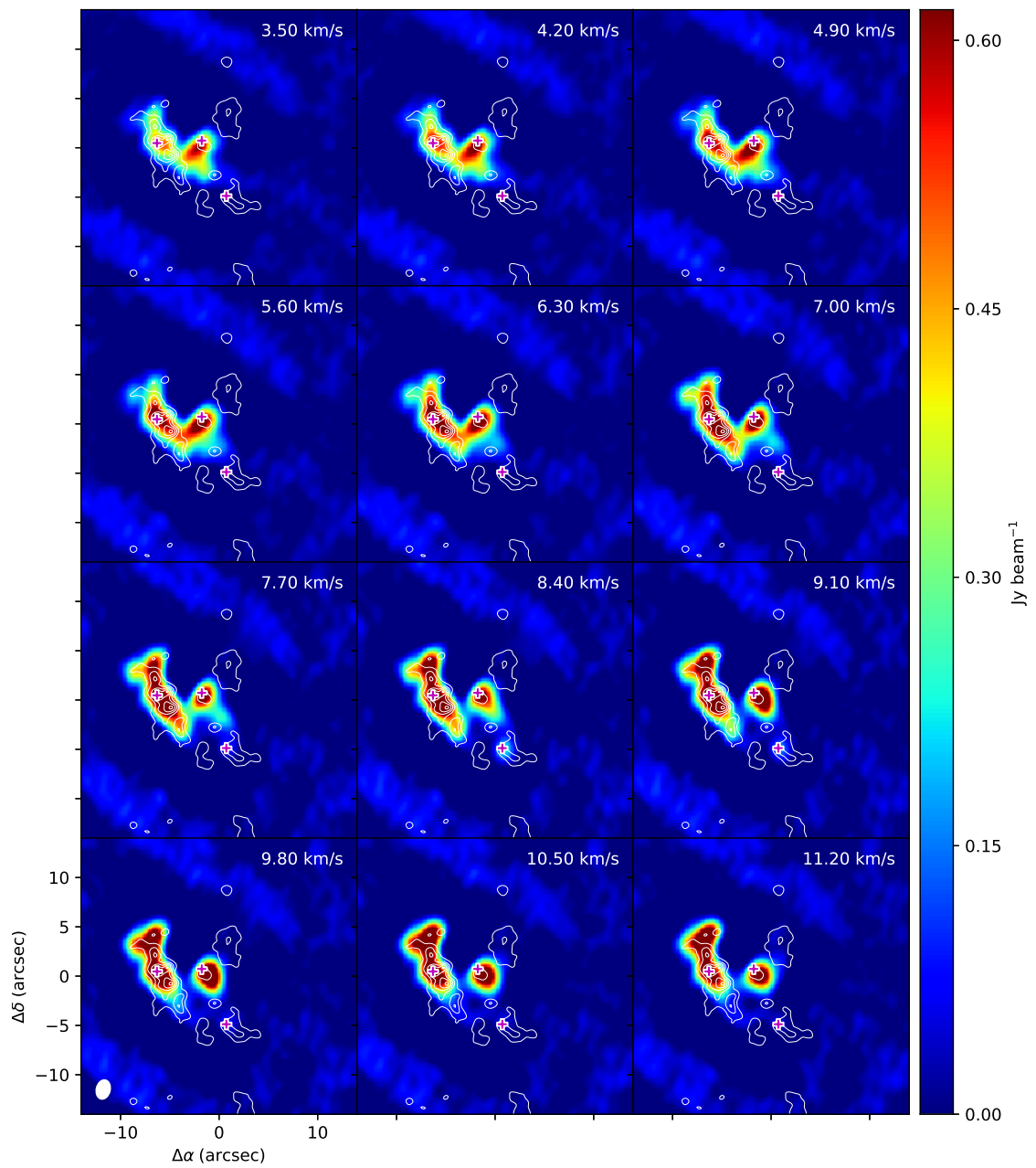


Figure B.5: 227.545GHz

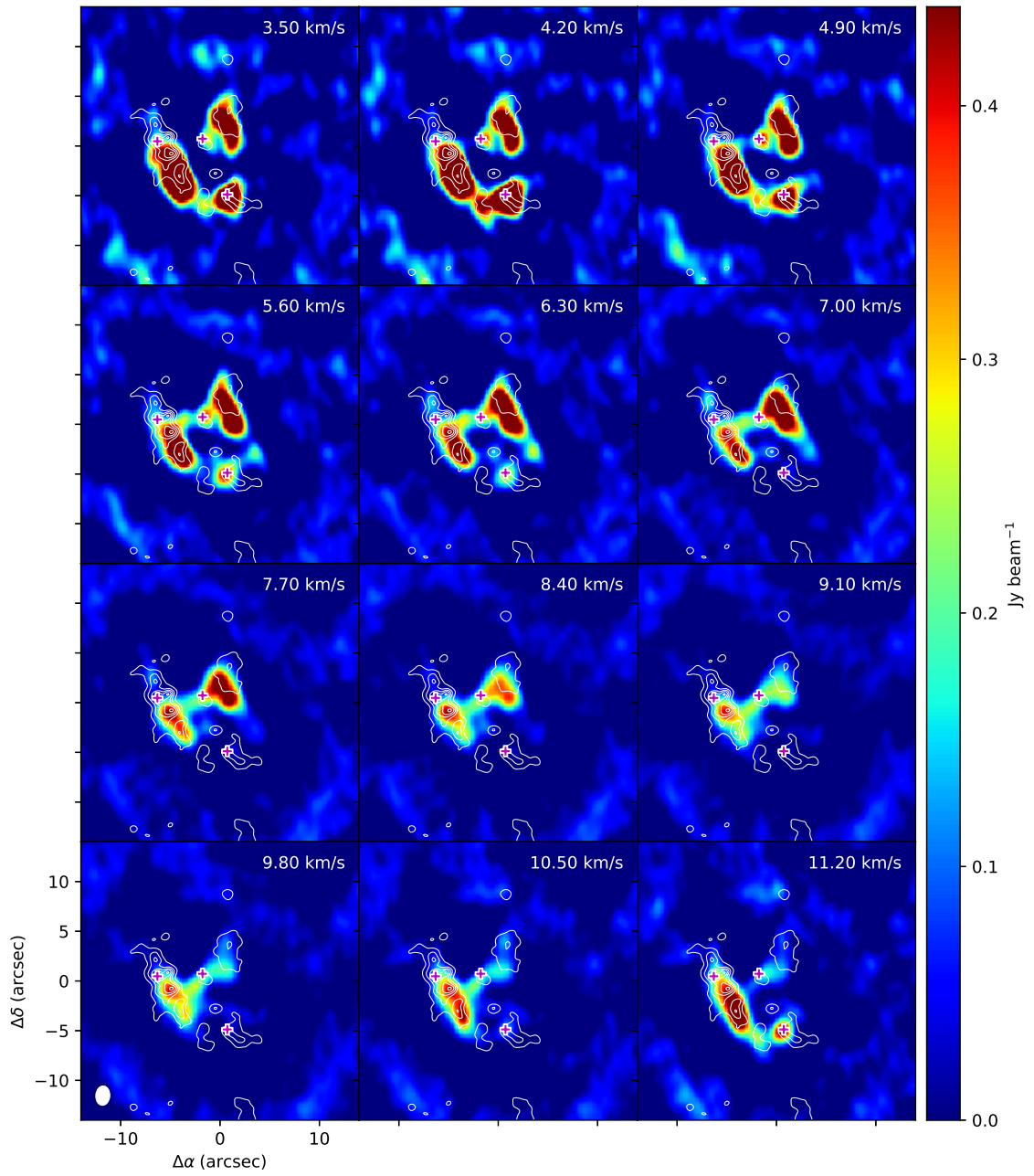


Figure B.6: 231.844GHz

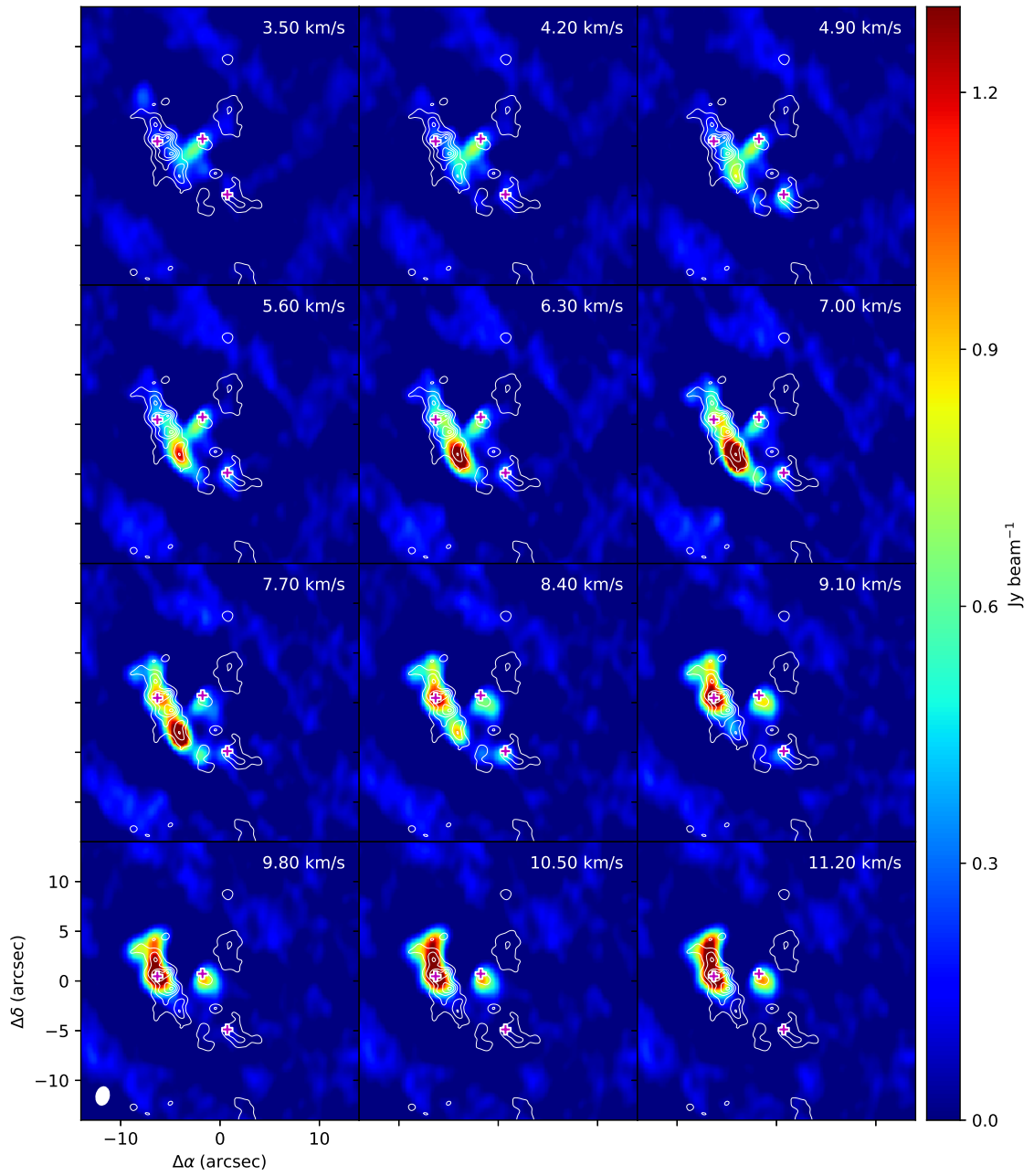


Figure B.7: 242.625GHz

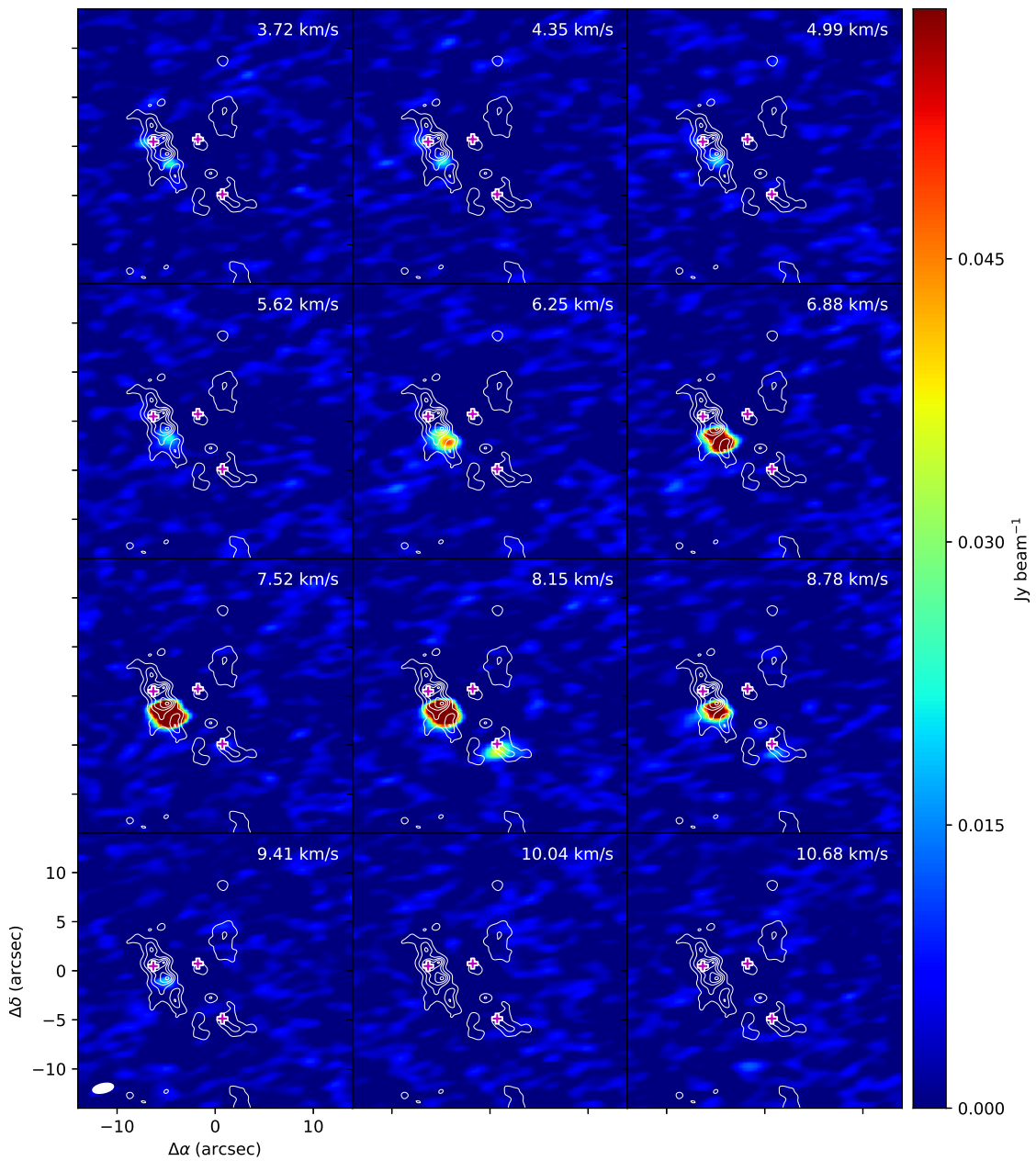


Figure B.8: 231.524GHz

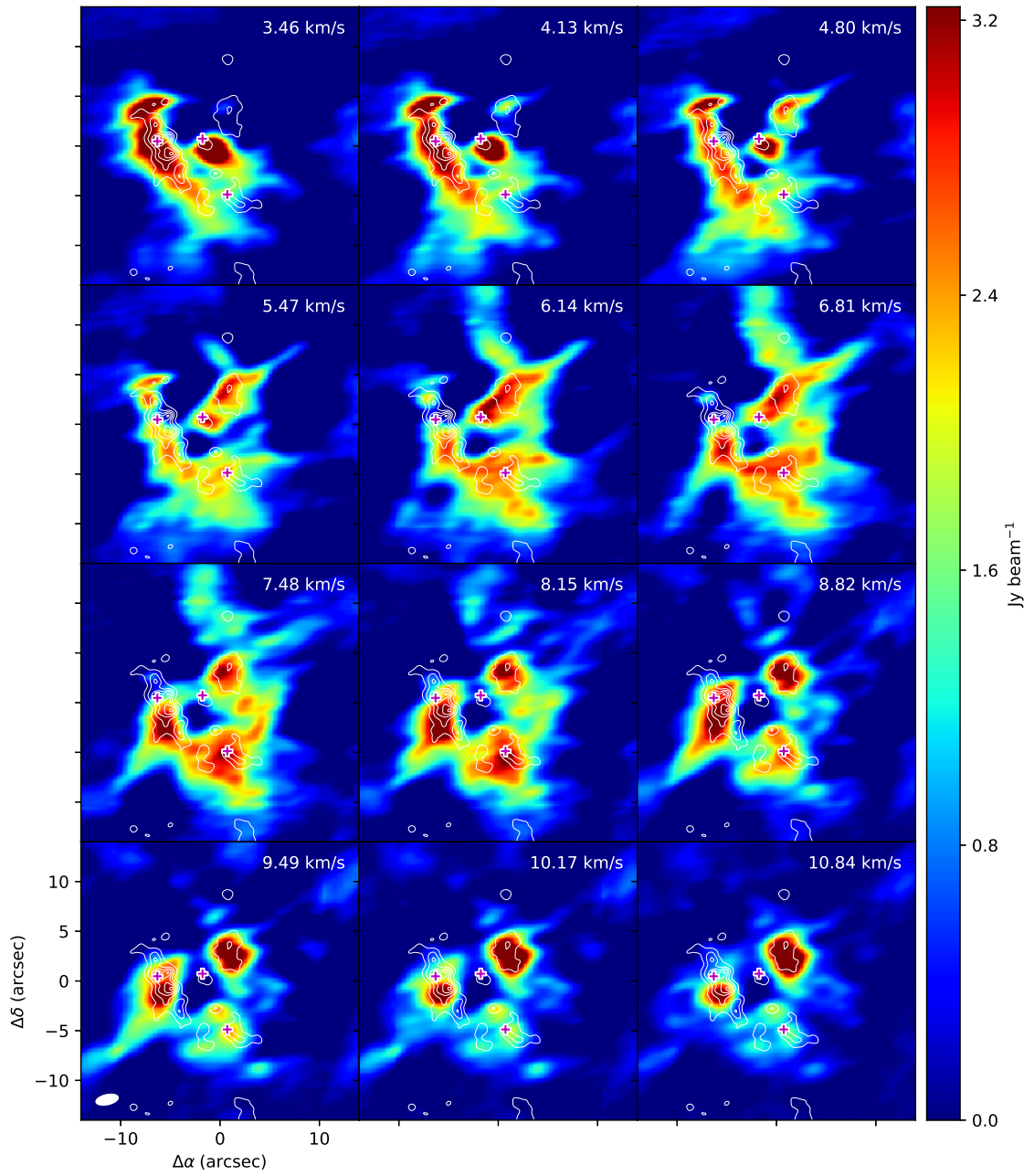


Figure B.9: 218.221GHz

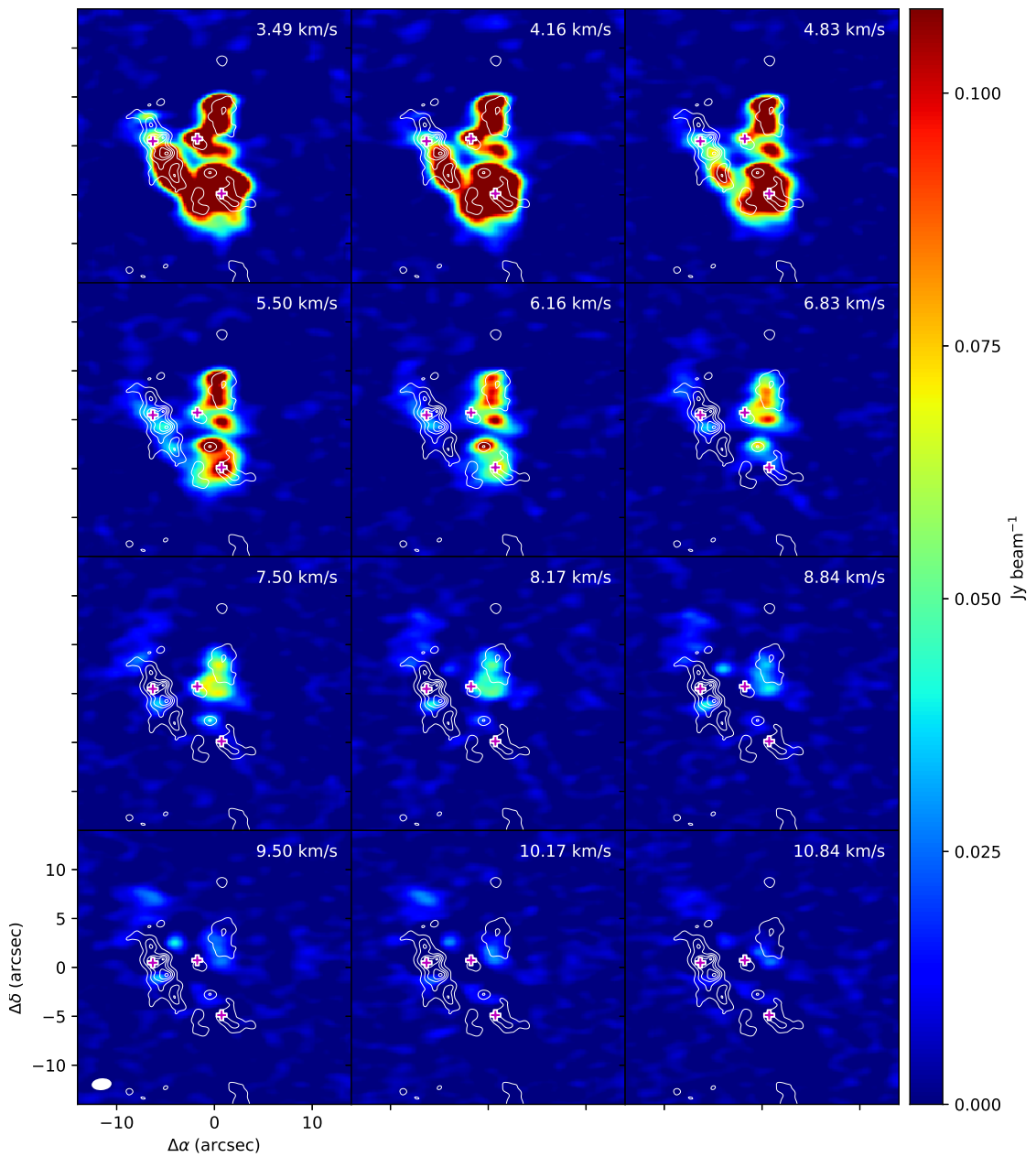


Figure B.10: 219.151GHz

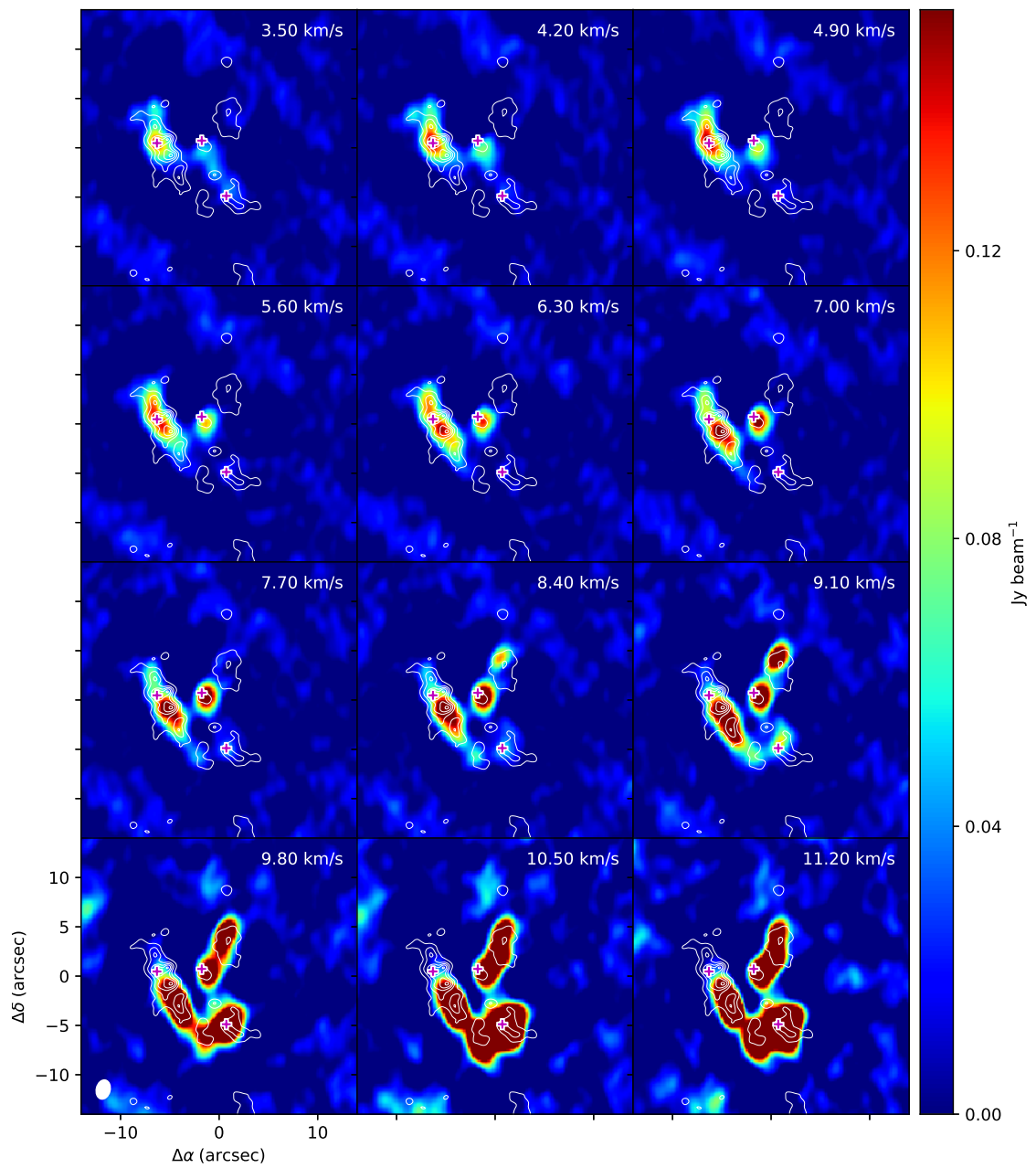


Figure B.11: 227.997GHz

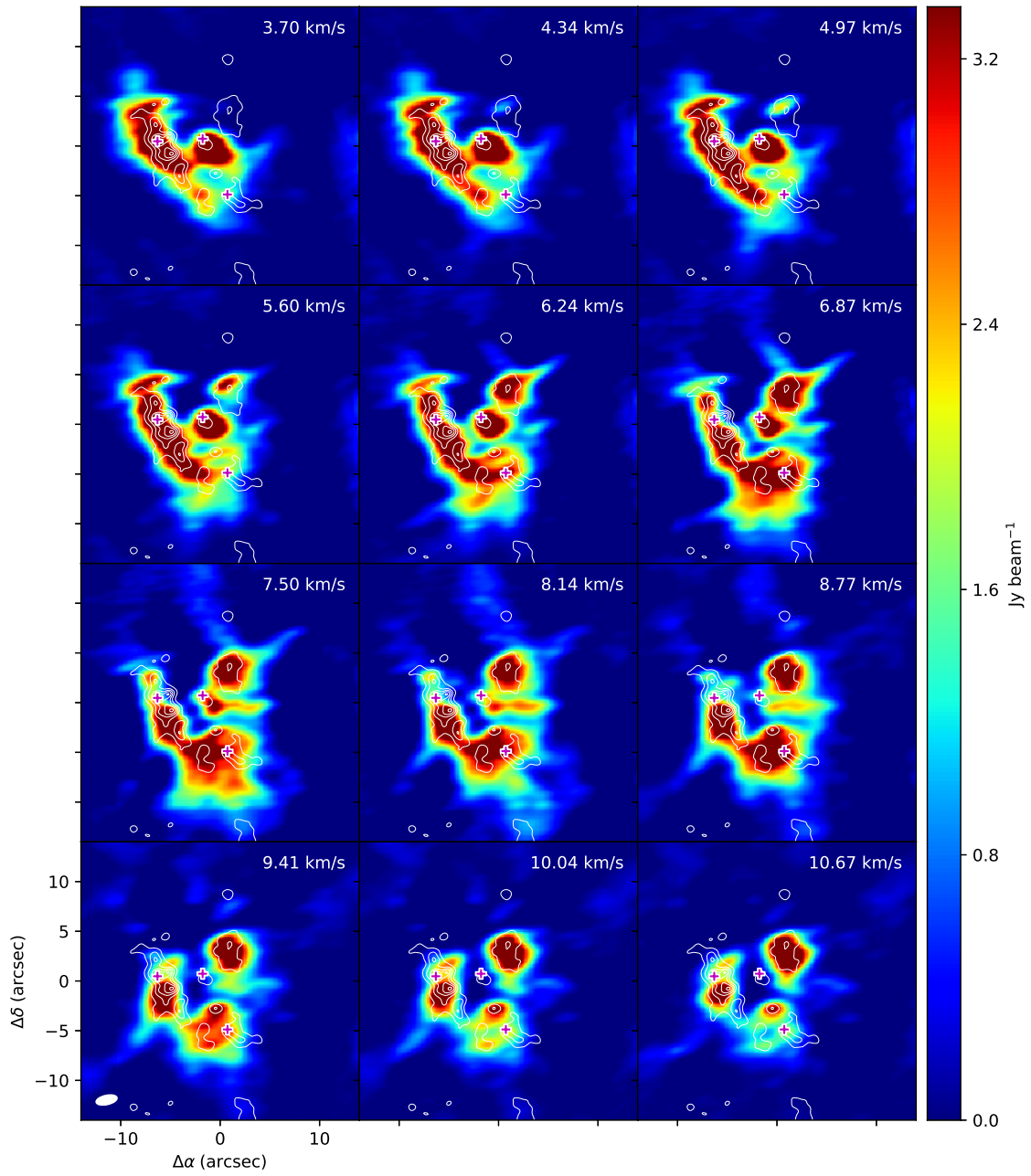


Figure B.12: 231.061GHz

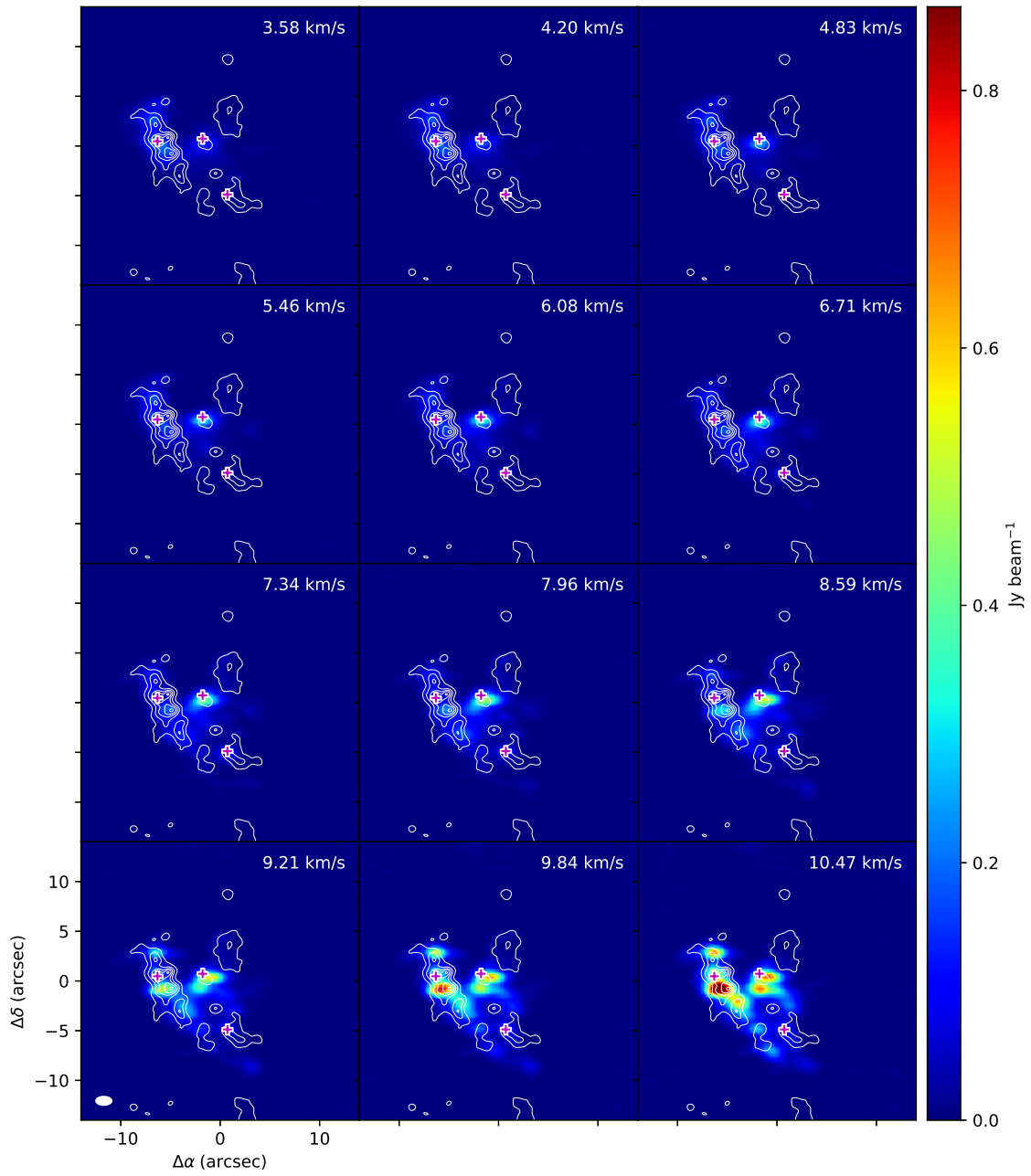


Figure B.13: 233.802GHz

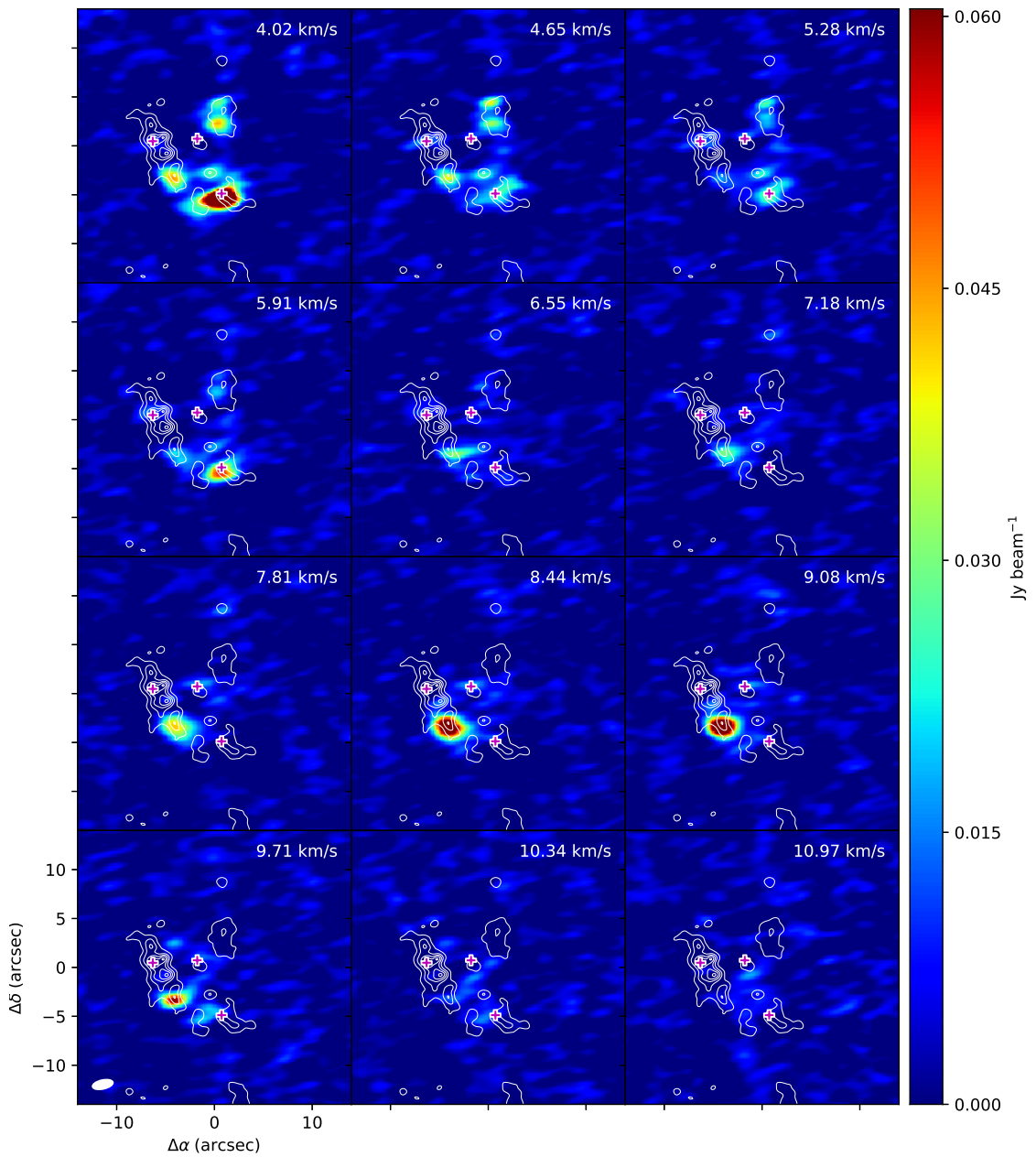


Figure B.14: 231.576GHz

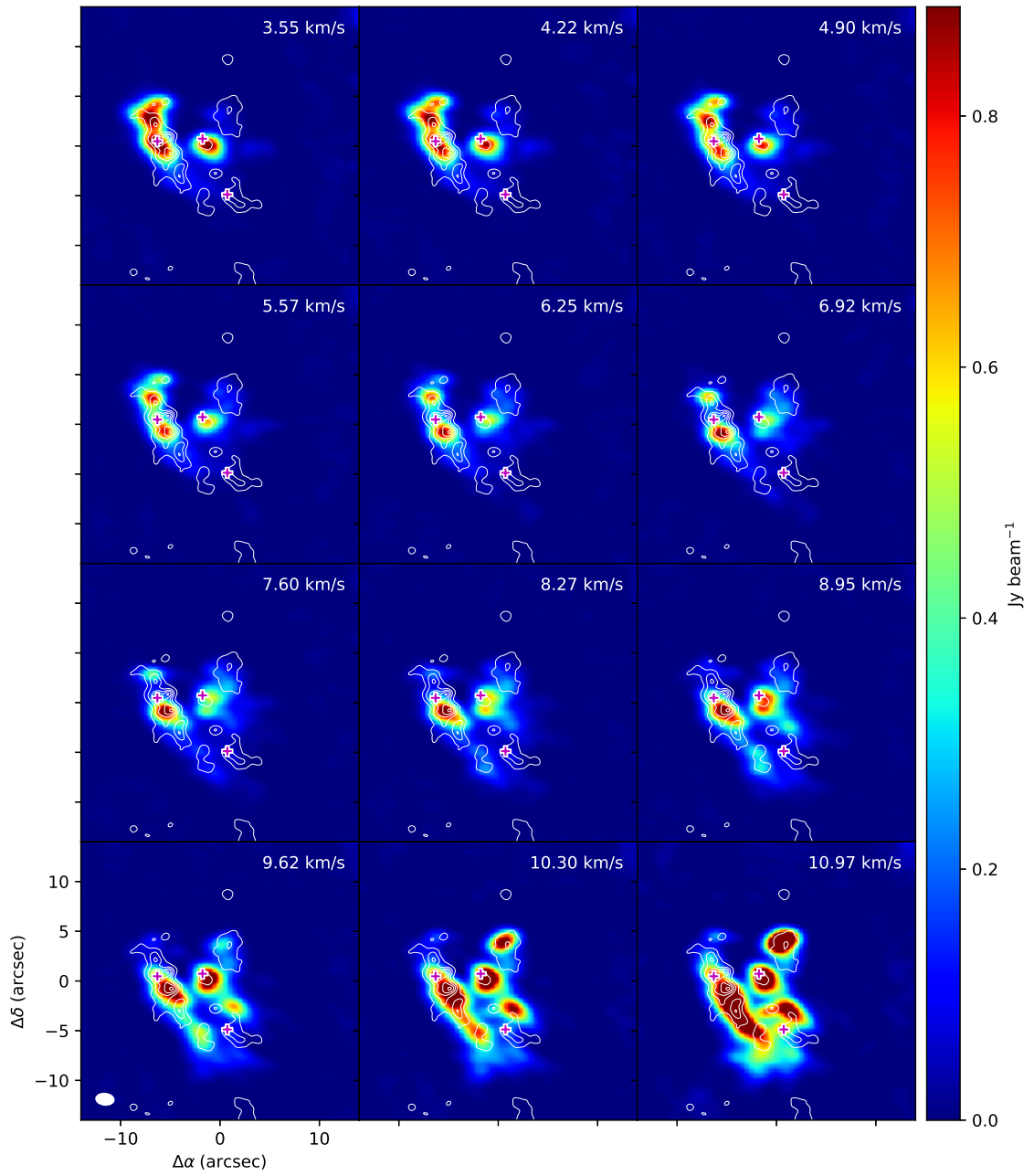


Figure B.15: 216.843GHz

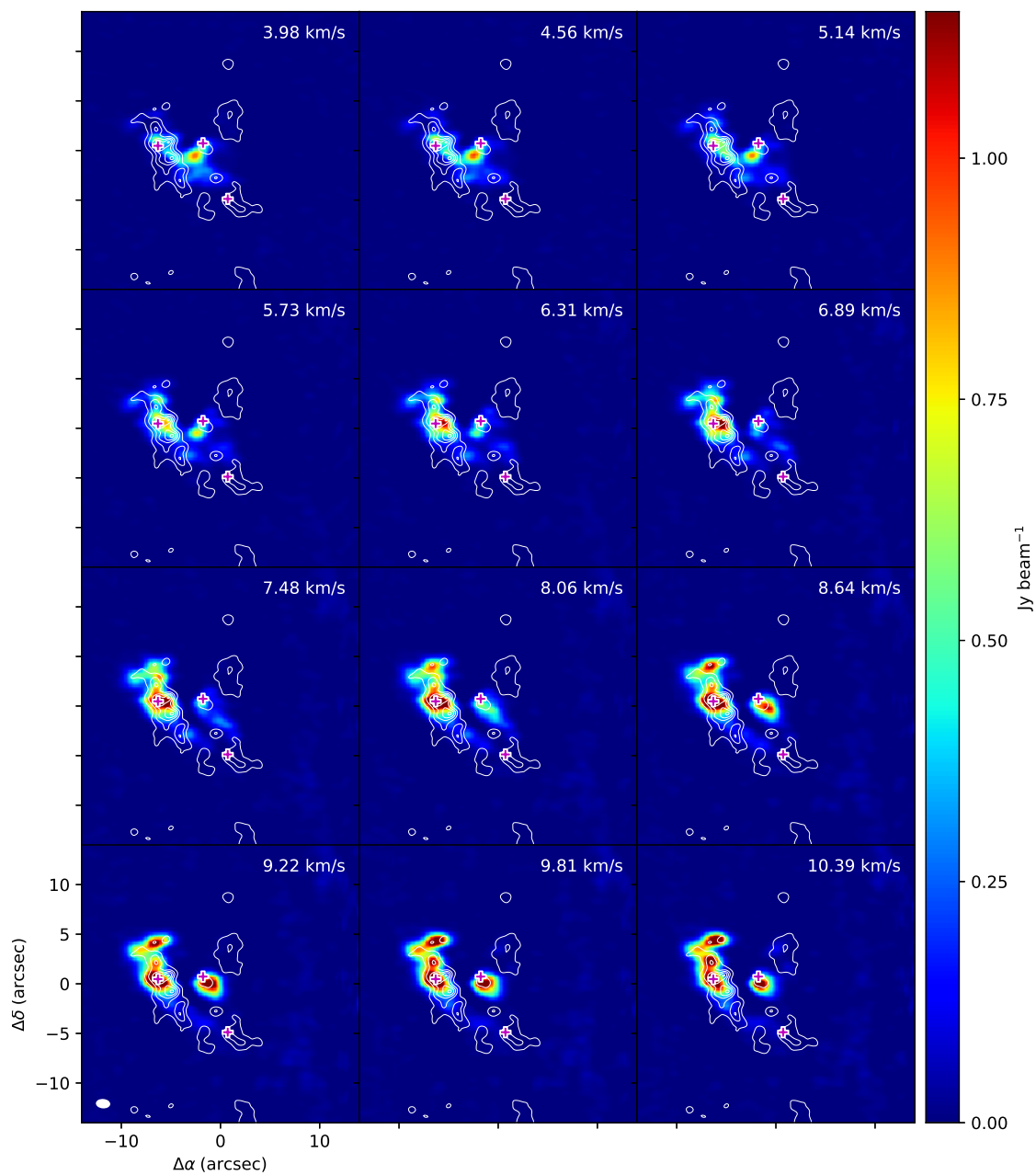


Figure B.16: 251.128GHz

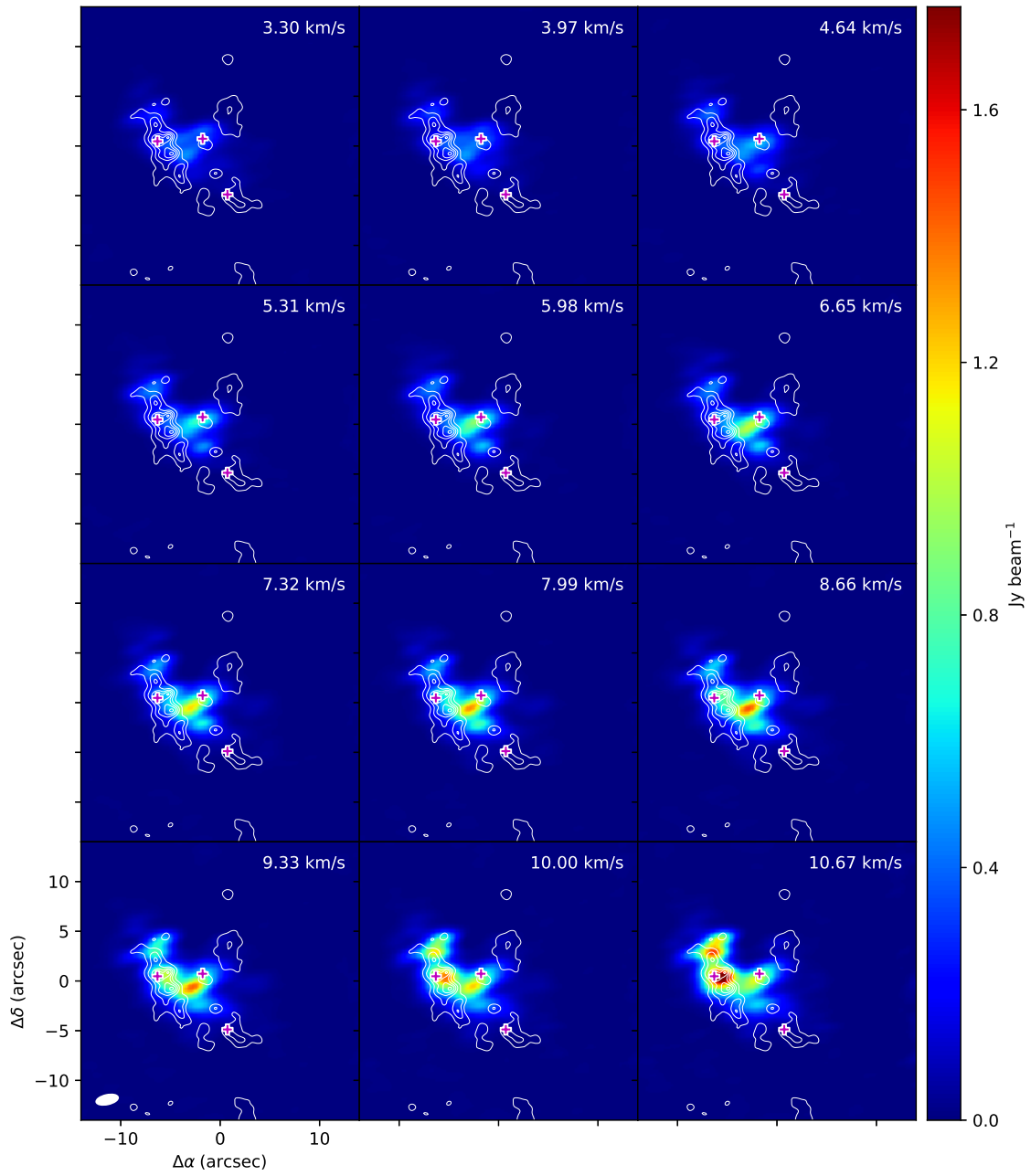


Figure B.17: 218.409GHz

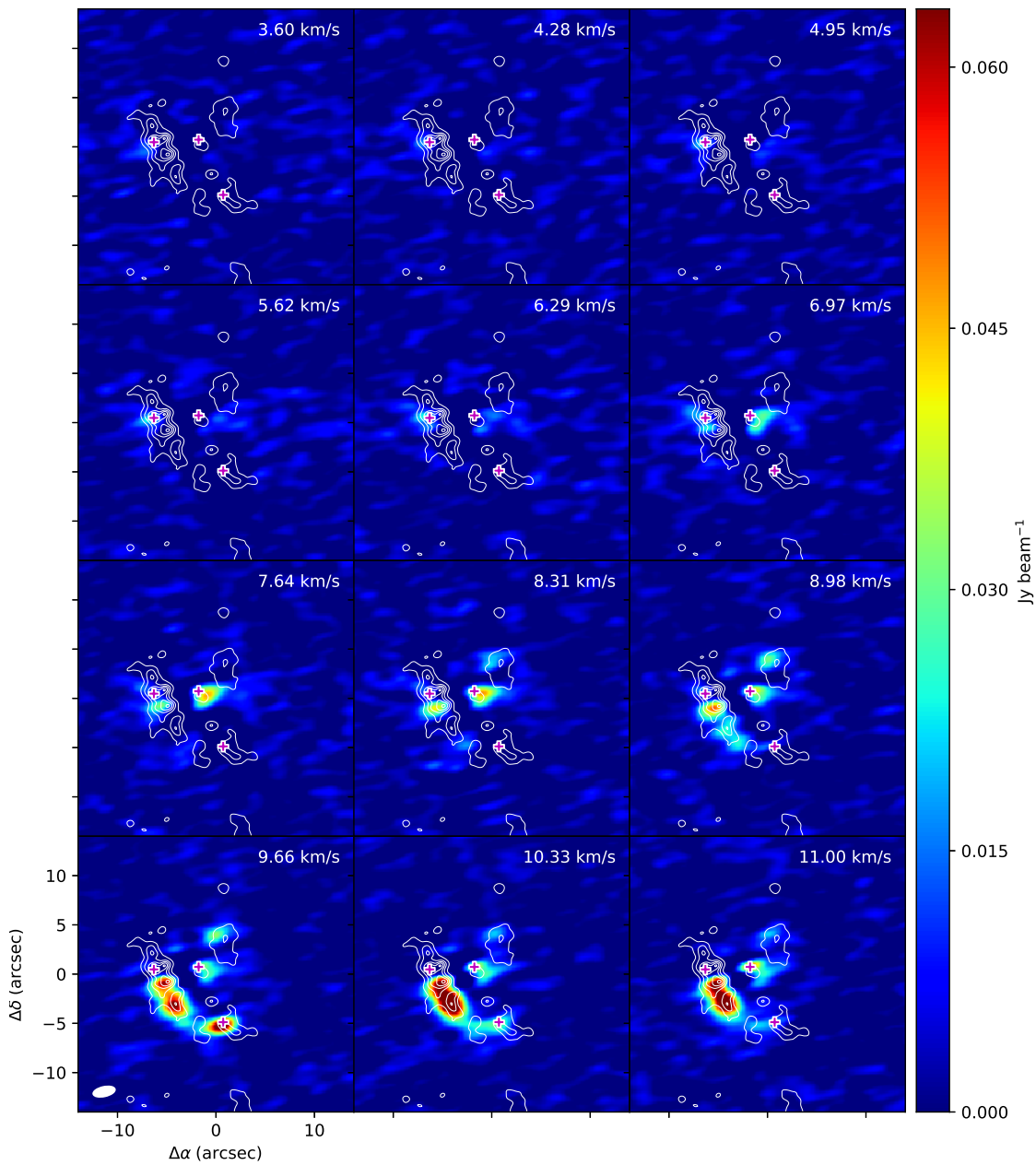


Figure B.18: 217.670GHz

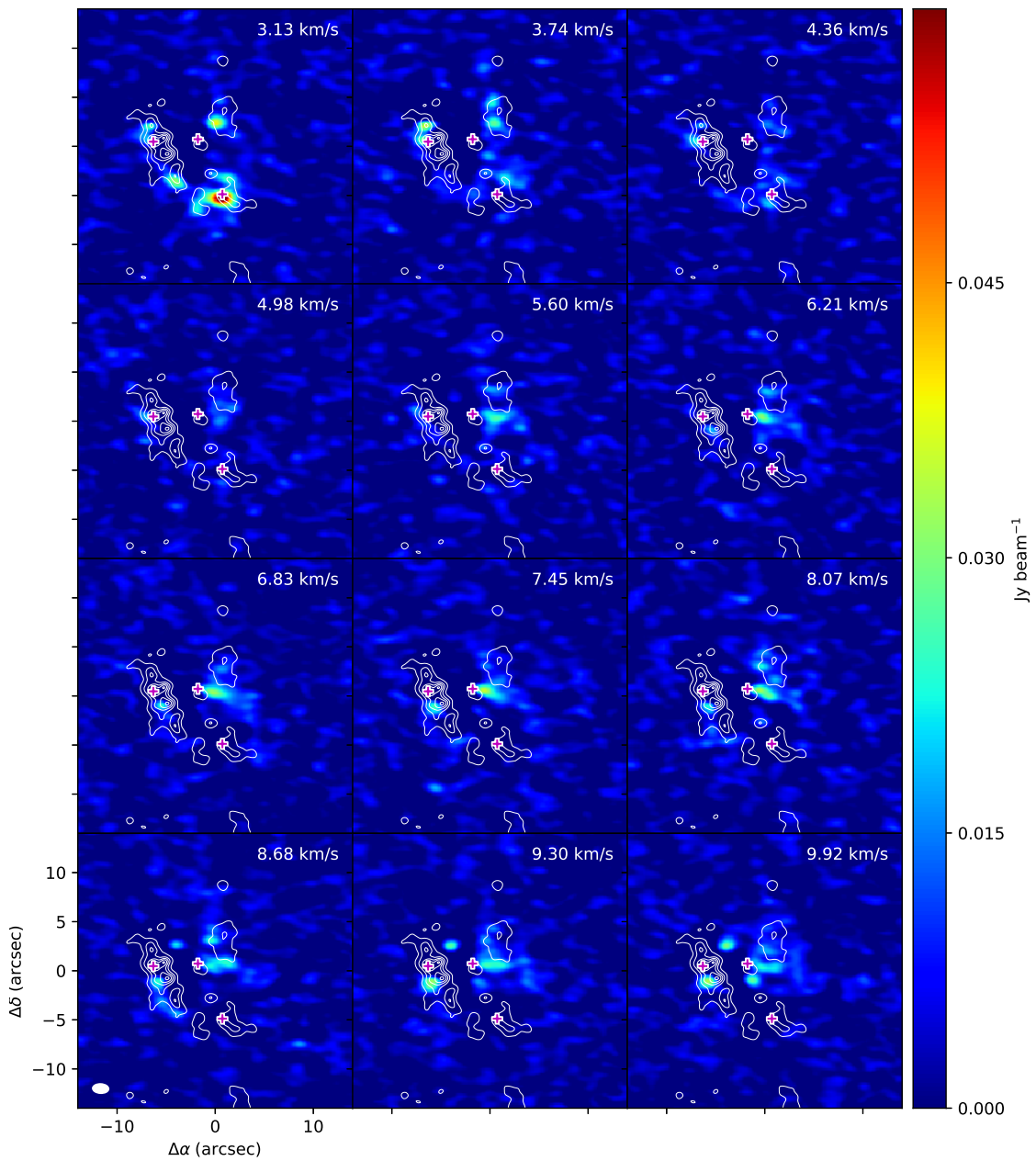


Figure B.19: 237.144GHz

Acknowledgments

This work would have been never completed if any one of greatest persons and colleagues mentioned below is missing.

I would like to express my gratitude my supervisor, Associate Professor Hideko Nomura, for her great directions, fruitful discussions, and persistent encouragement. I would like to do the same to Dr. Tomoya Hirota and Dr. Masatoshi Oh'ishi, who led me to the field of radio astronomy. As for the data analysis of the ALMA telescope, Dr. Yoko Oya, Dr. Toshiki Saito and Dr. Ryohei Kawabe gave me elaborate guidance. I also received generous warm support and comments from Dr. Taiki Suzuki, Seongjoong Kim, and Wei Chen-en.

Finally, I am grateful to all of the colleagues of planetary groups at Tokyo Tech, and the seminar mates of ALMA interferometer seminar at National Astronomical Observatory of Japan (NAOJ) for scientific discussion and enjoyable life.

References

- Altwegg, K., et al. 2016, *Science Advances*, 2, e1600285
- . 2017, *Monthly Notices of the Royal Astronomical Society*, 469, S130
- Bossa, J.-B., Duvernay, F., Theulé, P., Borget, F., D'Hendecourt, L., & Chiavassa, T. 2009, *Astronomy & Astrophysics*, 506, 601
- Ehrenfreund, P., Bernstein, M. P., Dworkin, J. P., Sandford, S. A., & Allamandola, L. J. 2001, *The Astrophysical Journal Letters*, 550, L95
- Feng, S., Beuther, H., Henning, T., Semenov, D., Palau, A., & Mills, E. A. C. 2015, *Astronomy & Astrophysics*, 581, A71
- Fourikis, N., Takagi, K., & Morimoto, M. 1974, *The Astrophysical Journal Letters*, 191, L139
- Glavin, D. P., Dworkin, J. P., & Sandford, S. A. 2008, *Meteoritics and Planetary Science*, 43, 399
- Gong, Y., et al. 2015, *Astronomy & Astrophysics*, 581, A48
- Hirota, T., Kim, M. K., Kurono, Y., & Honma, M. 2015, *The Astrophysical Journal*, 801, 82
- Holtom, P. D., Bennett, C. J., Osamura, Y., Mason, N. J., & Kaiser, R. I. 2005, *The Astrophysical Journal*, 626, 940

- Kaifu, N., Morimoto, M., Nagane, K., Akabane, K., Iguchi, T., & Takagi, K. 1974, The Astrophysical Journal Letters, 191, L135
- Kounkel, M., et al. 2017, The Astrophysical Journal, 834, 142
- Lee, C.-W., Kim, J.-K., Moon, E.-S., Minh, Y. C., & Kang, H. 2009, The Astrophysical Journal, 697, 428
- McMullin, J. P., Waters, B., Schiebel, D., Young, W., & Golap, K. 2007, in Astronomical Society of the Pacific Conference Series, Vol. 376, Astronomical Data Analysis Software and Systems XVI, ed. R. A. Shaw, F. Hill, & D. J. Bell, 127
- Motiyenko, R. A., Ilyushin, V. V., Drouin, B. J., Yu, S., & Margulès, L. 2014, Astronomy & Astrophysics, 563, A137
- Pagani, L., Favre, C., Goldsmith, P. F., Bergin, E. A., Snell, R., & Melnick, G. 2017, Astronomy & Astrophysics, 604, A32
- Sanchez-Monge, A., Schilke, P., Ginsburg, A., Cesaroni, R., & Schmiedeke, A. 2017, STATCONT: Statistical continuum level determination method for line-rich sources, Astrophysics Source Code Library
- Turner, B. E. 1991, The Astrophysical Journal Supplement, 76, 617